

Probing spin hydrodynamics on a superconducting quantum simulator

Yun-Hao Shi,^{1,2,3,*} Zheng-Hang Sun,^{1,2,*} Yong-Yi Wang,^{1,2,*} Zheng-An Wang,^{3,4} Yu-Ran Zhang,⁵ Wei-Guo Ma,^{1,2} Hao-Tian Liu,^{1,2} Kui Zhao,³ Jia-Cheng Song,^{1,2} Gui-Han Liang,^{1,2} Zheng-Yang Mei,^{1,2} Jia-Chi Zhang,^{1,2} Hao Li,³ Chi-Tong Chen,^{1,2} Xiaohui Song,¹ Jieci Wang,⁶ Guangming Xue,³ Haifeng Yu,³ Kaixuan Huang,^{3,†} Zhongcheng Xiang,^{1,2,4,‡} Kai Xu,^{1,2,3,4,7,8,§} Dongning Zheng,^{1,2,4,7,8} and Heng Fan^{1,2,3,4,7,8,¶}

¹*Institute of Physics, Chinese Academy of Sciences, Beijing 100190, China*

²*School of Physical Sciences, University of Chinese Academy of Sciences, Beijing 100049, China*

³*Beijing Academy of Quantum Information Sciences, Beijing 100193, China*

⁴*Hefei National Laboratory, Hefei 230088, China*

⁵*School of Physics and Optoelectronics, South China University of Technology, Guangzhou 510640, China*

⁶*Department of Physics and Key Laboratory of Low Dimensional Quantum Structures and Quantum Control of Ministry of Education, Hunan Normal University, Changsha, Hunan 410081, China*

⁷*Songshan Lake Materials Laboratory, Dongguan, Guangdong 523808, China*

⁸*CAS Center for Excellence in Topological Quantum Computation, UCAS, Beijing 100190, China*

Characterizing the nature of hydrodynamical transport properties in quantum dynamics provides valuable insights into the fundamental understanding of exotic non-equilibrium phases of matter. Experimentally simulating infinite-temperature transport on large-scale complex quantum systems is of considerable interest. Here, using a controllable and coherent superconducting quantum simulator, we experimentally realize the analog quantum circuit, which can efficiently prepare the Haar-random states, and probe spin transport at infinite temperature. We observe diffusive spin transport during the unitary evolution of the ladder-type quantum simulator with ergodic dynamics. Moreover, we explore the transport properties of the systems subjected to strong disorder or a tilted potential, revealing signatures of anomalous subdiffusion in accompany with the breakdown of thermalization. Our work demonstrates a scalable method of probing infinite-temperature spin transport on analog quantum simulators, which paves the way to study other intriguing out-of-equilibrium phenomena from the perspective of transport.

Introduction

Transport properties of quantum many-body systems driven out of equilibrium are of significant interest in several active areas of modern physics, including the ergodicity of quantum systems [1–4] and quantum magnetism [5–7]. Understanding these properties is crucial to unveil the non-equilibrium dynamics of isolated quantum systems [8, 9]. One essential property of transport is the emergence of classical hydrodynamics in microscopic quantum dynamics, which shows the power-law tail of autocorrelation functions [8]. The rate of the power-law decay, referred as to the transport exponent, characterizes the universal classes of hydrodynamics. In d -dimensional quantum systems, in addition to generally expected diffusive transport with the exponent $d/2$ in non-integrable systems [10–12], more attentions have been attracted by the anomalous superdiffusive [5, 13–16] or subdiffusive transport [2, 3, 17–19], with the exponent larger or smaller than $d/2$, respectively.

Over the last few decades, considerable strides have been made in enhancing the scalability, controllability, and coherence of noisy intermediate-scale quantum (NISQ) devices based on superconducting qubits [20–23]. With these advancements, several novel phenomena in non-equilibrium dynamics of quantum many-body systems have been observed, such as quantum thermalization [24, 25], ergodicity breaking [26–29], time crystal [30–32], and information scrambling [33, 34]. More importantly, in this platform, the beyond-classical computation has been demonstrated by sampling the final Haar-random states of randomized sequences of gate operations [35–39]. Recently, a method of measuring autocorrelation functions at infinite temperature based on the Haar-random states has been proposed, which opens up a practical application of pseudo-random quantum circuits for simulating hydrodynamics on NISQ devices [40, 41].

In this work, using a ladder-type superconducting quantum simulator with up to 24 qubits, we first demonstrate that in addition to the digital pseudo-random circuits [35–41], a unitary evolution governed by a time-independent Hamiltonian, i.e., an analog quantum circuit, can also generate quantum states randomly chosen from the Haar measure, i.e., the Haar-random states, for measuring the infinite-temperature autocorrelation functions [42–44]. Subsequently, we study the properties of

* These authors contributed equally to this work.

† huangkx@baqis.ac.cn

‡ zcxiang@iphy.ac.cn

§ kaixu@iphy.ac.cn

¶ hfan@iphy.ac.cn

spin transport on the superconducting quantum simulator via the measurement of autocorrelation functions by using the Haar-random states. Notably, we observe a clear signature of the diffusive transport on the qubit ladder, which is a non-integrable system [11, 12, 25].

Upon subjecting the qubit ladder to disorder, a transition from delocalized phases to the many-body localization (MBL) occurs as the strength of disorder increases [45]. By measuring the autocorrelation functions, we experimentally probe an anomalous subdiffusive transport with intermediate values of the disorder strength. The observed signs of subdiffusion are consistent with recent numerical results, and can be explained as a consequence of Griffith-like region on the delocalized side of the MBL transition [2, 3, 46–49].

Finally, we explore spin transport on the qubit ladder with a linear potential, and it is expected that Stark MBL occurs when the potential gradients are sufficiently large [28, 50–54]. With a large gradient, the conservation of the dipole moment emerges [28, 54], associated with the phenomena known as the Hilbert space fragmentation [55–57]. Recent theoretical works reveal a subdiffusion in the dipole-moment conserving systems [17, 19]. In this experiment, we present evidence of a subdiffusive regime of spin transport in the tilted qubit ladder.

Results

Experimental setup and protocol

Our experiments are performed on a programmable superconducting quantum simulator, consisting of 30 transmon qubits with a geometry of two-legged ladder, see Fig. 1a and b. The nearest-neighbor qubits are coupled by a fixed capacitor, and the effective Hamiltonian of capacitive interactions can be written as [22, 23] (also see Supplementary Note 1)

$$\begin{aligned} \hat{H}_I/\hbar = & \sum_{m \in \{\uparrow, \downarrow\}} \sum_{j=1}^{L-1} J_{j,m}^{\parallel} (\hat{\sigma}_{j,m}^+ \hat{\sigma}_{j+1,m}^- + \text{H.c.}) \\ & + \sum_{j=1}^L J_j^{\perp} (\hat{\sigma}_{j,\uparrow}^+ \hat{\sigma}_{j,\downarrow}^- + \text{H.c.}), \end{aligned} \quad (1)$$

where $\hbar = h/2\pi$, with h being the Planck constant (in the following we set $\hbar = 1$), L is the length of the ladder, $\hat{\sigma}_{j,m}^+$ ($\hat{\sigma}_{j,m}^-$) is the raising (lowering) operator for the qubit $Q_{j,m}$, and $J_{j,m}^{\parallel}$ (J_j^{\perp}) refers to the rung (intrachain) hopping strength. For this device, the averaged rung and intrachain hopping strength are $\overline{J^{\parallel}}/2\pi \simeq 7.3$ MHz and $\overline{J^{\perp}}/2\pi \simeq 6.6$ MHz, respectively. The XY and Z control lines on the device enable us to realize the drive Hamiltonian $\hat{H}_d = \sum_{m \in \{\uparrow, \downarrow\}} \sum_{j=1}^L \Omega_{j,m} (e^{-i\phi_{j,m}} \hat{\sigma}_{j,m}^+ + e^{i\phi_{j,m}} \hat{\sigma}_{j,m}^-)/2$, and the on-site potential Hamiltonian $\hat{H}_Z = \sum_{m \in \{\uparrow, \downarrow\}} \sum_{j=1}^L w_{j,m} \hat{\sigma}_{j,m}^+ \hat{\sigma}_{j,m}^-$, respectively. Here,

$\Omega_{j,m}$ and $\phi_{j,m}$ denote the driving amplitude and the phase of the microwave pulse applied on the qubit $Q_{j,m}$, and $w_{j,m}$ is the effective on-site potential.

To study spin transport and hydrodynamics, we focus on the equal-site autocorrelation function at infinite temperature, which is defined as

$$C_{\mathbf{r},\mathbf{r}} = \frac{1}{D} \text{Tr}[\hat{\rho}_{\mathbf{r}}(t)\hat{\rho}_{\mathbf{r}}], \quad (2)$$

where $\hat{\rho}_{\mathbf{r}}$ is a local observable at site \mathbf{r} , $\hat{\rho}_{\mathbf{r}}(t) = e^{i\hat{H}t} \hat{\rho}_{\mathbf{r}} e^{-i\hat{H}t}$, and D is the Hilbert dimension of the Hamiltonian \hat{H} . Here, for the ladder-type superconducting simulator, we choose $\hat{\rho}_{\mathbf{r}} = (\hat{\sigma}_{1,\uparrow}^z + \hat{\sigma}_{1,\downarrow}^z)/2$ ($\mathbf{r} = 1$) [12], and the autocorrelation function can be rewritten as

$$C_{1,1} = \frac{1}{4} (c_{1,\uparrow;1,\uparrow} + c_{1,\uparrow;1,\downarrow} + c_{1,\downarrow;1,\uparrow} + c_{1,\downarrow;1,\downarrow}), \quad (3)$$

with $c_{\mu;\nu} = \text{Tr}[\hat{\sigma}_{\mu}^z(t)\hat{\sigma}_{\nu}^z]/D$ (subscripts μ and ν denote the qubit index 1, \uparrow or 1, \downarrow).

The autocorrelation functions (2) at infinite temperature can be expanded as the average of $C_{\mathbf{r},\mathbf{r}}(|\psi_0\rangle) = \langle \psi_0 | \hat{\rho}_{\mathbf{r}}(t) \hat{\rho}_{\mathbf{r}} | \psi_0 \rangle$ over different $|\psi_0\rangle$ in z -basis. In fact, the dynamical behavior of an individual $C_{\mathbf{r},\mathbf{r}}(|\psi_0\rangle)$ is sensitive to the choice of $|\psi_0\rangle$ under some circumstances (see Supplementary Note 7 for the dependence of $C_{\mathbf{r},\mathbf{r}}(|\psi_0\rangle)$ on $|\psi_0\rangle$ in the qubit ladder with a linear potential as an example). To experimentally probe the generic properties of spin transport at infinite temperature, one can obtain (2) by measuring and averaging $C_{\mathbf{r},\mathbf{r}}(|\psi_0\rangle)$ with different $|\psi_0\rangle$ [15]. Alternatively, we employ a more efficient method to measure (2) without the need of sampling different $|\psi_0\rangle$. Based on the results in ref. [40] (also see Methods), the autocorrelation function $c_{\mu;\nu}$ can be indirectly measured by using the quantum circuit as shown in Fig. 1c, i.e.,

$$c_{\mu;\nu} \simeq \langle \psi_{\nu}^R(t) | \hat{\sigma}_{\mu}^z | \psi_{\nu}^R(t) \rangle, \quad (4)$$

where $|\psi_{\nu}^R(t)\rangle = \hat{U}_H(t)[|0\rangle_{\nu} \otimes |\psi^R\rangle]$ with $|\psi^R\rangle = \hat{U}_R \otimes_{i \in Q_R} |0\rangle_i$, and \hat{U}_R being a unitary evolution generating Haar-random states. For example, to experimentally obtain $c_{1,\downarrow;1,\uparrow}$, we choose $Q_{1,\uparrow}$ as Q_A , and the remainder qubits as the Q_R . After performing the pulse sequences as shown in Fig. 1d, we measure the qubit $Q_{1,\downarrow}$ at z -basis to obtain the expectation value of the observable $\hat{\sigma}_{1,\downarrow}^z$.

Observation of diffusive transport

In this experiment, we first study spin transport on the 24-qubit ladder consisting of $Q_{1,\uparrow}, \dots, Q_{12,\uparrow}$ and $Q_{1,\downarrow}, \dots, Q_{12,\downarrow}$, described by the Hamiltonian (1). For a non-integrable model, one expects that diffusive transport $C_{1,1} \propto t^{-1/2}$ occurs [12]. To measure the autocorrelation

function $C_{1,1}$ defined in Eq. (3), we should first perform a quantum circuit generating the required Haar-random states $|\psi^R\rangle$. Instead of using the digital pseudo-random circuits in Refs. [35–41], here we experimentally realize the time evolution under the Hamiltonian $\hat{H}_R = \hat{H}_I + \hat{H}_d$, where the parameters $\Omega_{j,m}$ and $\phi_{j,m}$ in \hat{H}_d have site-dependent values with the average $\bar{\Omega}/2\pi \simeq 10.4$ MHz ($\bar{\Omega}/J \simeq 1.4$) and $\bar{\phi} = 0$ (see Methods and Supplementary Note 3 for more details), i.e., $\hat{U}_R(t_R) = \exp(-i\hat{H}_R t_R)$, which is more suitable for our analog quantum simulator. To benchmark that the final state $|\psi^R\rangle = \hat{U}_R(t_R)|0\rangle$ can approximate the Haar-random states, we measure the participation entropy $S_{PE} = -\sum_{k=1}^D p_k \ln p_k$, with D being the dimension of Hilbert space, $p_k = |\langle k|\psi^R\rangle|^2$, and $\{|k\rangle\}$ being a computational basis. Figure 2a shows the results of S_{PE} with different evolution times t_R . For the 23-qubit system, the probabilities p_k are estimated from the single-shot readout with a number of samples $N_s = 3 \times 10^7$. It is seen that the S_{PE} tends to the value for Haar-random states, i.e., $S_{PE}^T = N \ln 2 - 1 + \gamma$ with $N = 23$ being the number of qubits and $\gamma \simeq 0.577$ as the Euler's constant [36]. Moreover, for the final state $|\psi^R\rangle$ with $t_R = 200$ ns, the distribution of probabilities p_k satisfies the Porter-Thomas distribution (see Supplementary Note 4).

In Fig. 2b, we show the dynamics of the autocorrelation function $C_{1,1}$ measured via the quantum circuit in Fig. 1c with $t_R = 200$ ns. The experimental data satisfies $C_{1,1} \propto t^{-\alpha}$, with a transport exponent $\alpha \simeq 0.5067$, estimated by fitting the data in the time window $t \in [50 \text{ ns}, 200 \text{ ns}]$. Our experiments clearly show that spin diffusively transports on the qubit ladder \hat{H}_I (1), and demonstrate that the analog quantum circuit $\hat{U}_R(t_R)$ with $t_R = 200$ ns can provide sufficient randomness to measure the autocorrelation function defined in Eq. (2) and probe infinite-temperature spin transport. We also discuss the influence of t_R in Supplementary Note 4, numerically showing that the results of $C_{1,1}$ do not substantially change for longer $t_R > 200$ ns. Moreover, in Supplementary Note 4, we show that for a short evolved time $t_R \simeq 15$ ns, the values of the observable defined in Eq. (4) are incompatible with the infinite-temperature autocorrelation functions. Given that the chosen initial state for generating the Haar-random state exhibits a high effective temperature associated with the Hamiltonian \hat{H}_R , the state $|\psi^R\rangle$ would asymptotically converge to the Haar-random state with a sufficiently extended t_R . However, with $t_R \simeq 15$ ns, the time scale is too small to get rid of the coherence, and the value of S_{PE} for the state $|\psi^R\rangle$ is much smaller than the S_{PE}^T (see Fig. 2a), suggesting that $|\psi^R\rangle$ with $t_R \simeq 15$ ns is far away from the Haar-random state, and cannot be employed to measure the infinite-temperature autocorrelation function (2). In the follow-

ing, we fix $t_R = 200$ ns, and study spin transport in other systems with ergodicity breaking.

Subdiffusive transport with ergodicity breaking

After demonstrating that the quantum circuit shown in Fig. 1c can be employed to measure the infinite-temperature autocorrelation function $C_{1,1}$, we study spin transport on the superconducting qubit ladder with disorder, whose effective Hamiltonian can be written as $\hat{H}_D = \hat{H}_I + \sum_{m \in \{\uparrow, \downarrow\}} \sum_{j=1}^L w_{j,m} \hat{\sigma}_{j,m}^+ \hat{\sigma}_{j,m}^-$, with $w_{j,m}$ drawn from a uniform distribution $[-W, W]$, and W being the strength of disorder. For each disorder strength, we consider 10 disorder realizations and plot the dynamics of averaged $C_{1,1}$ with different W are plotted in Fig. 3a. With the increasing of W , and as the system approaches the MBL transition, $C_{1,1}$ decays more slowly. Moreover, the oscillation in the dynamics of $C_{1,1}$ becomes more obvious with larger W , which is related to the presence of local integrals of motion in the deep many-body localized phase [58].

We then fit both the experimental and numerical data with the time window $t \in [50 \text{ ns}, 200 \text{ ns}]$ by adopting the power-law decay $C_{1,1} \propto t^{-\alpha}$. As shown in Fig. 3b, we observe an anomalous subdiffusive region with the transport exponent $\alpha < 1/2$. For the strength of disorder $W/2\pi \gtrsim 50$ MHz, the transport exponent $\alpha \sim 10^{-2}$, indicating the freezing of spin transport and the onset of MBL on the 24-qubit system [2]. Here, we emphasize that the estimated transition point between the subdiffusive regime and MBL is a lower bound since with longer evolved time, the exponent α obtained from the power-law fitting becomes slightly larger (see Supplementary Note 6).

Next, we explore the transport properties on a tilted superconducting qubit ladder, which is subjected to the linear potential $\hat{H}_L = \sum_{j=1}^L \Delta j \sum_{m \in \{\uparrow, \downarrow\}} \hat{\sigma}_{j,m}^+ \hat{\sigma}_{j,m}^-$, with $\Delta = 2W_S/(L-1)$ being the slope of the linear potential (see the tilted ladder in the inset of Fig. 4a). Thus, the effective Hamiltonian of the tilted superconducting qubit ladder can be written as $\hat{H}_T = \hat{H}_I + \hat{H}_L$. Different from the aforementioned breakdown of ergodicity induced by the disorder, the non-ergodic behaviors induced by the linear potential arise from strong Hilbert-space fragmentation [55–57]. The ergodicity breaking in the disorder-free system \hat{H}_T is known as the Stark MBL [28, 50–54].

We employ the method based on the quantum circuit shown in Fig. 1c to measure the time evolution of the autocorrelation function $C_{1,1}$ with different slopes of the linear potential. The results are presented in Fig. 4a and 4b. Similar to the system with disorder, the dynamics of $C_{1,1}$ still satisfies $C_{1,1} \propto t^{-\alpha}$ with $\alpha < 0.5$, i.e., subdiffusive transport. Figure 4c displays the transport exponent α with different strength of the linear po-

tential, showing that α asymptotically drops as W_S increases.

Two remarks are in order. First, by employing the same standard for the onset of MBL induced by disorder, i.e., $\alpha \sim 10^{-2}$, the results in Fig. 4c indicate that the Stark MBL on the tilted 24-qubit ladder occurs when $W_S/2\pi \gtrsim 80$ MHz ($\Delta/2\pi \gtrsim 14.6$ MHz). Second, in the ergodic side ($W_S/2\pi < 80$ MHz and $W/2\pi < 50$ MHz for the tilted and disordered systems respectively), the transport exponent α exhibits rapid decay with increasing W_S up to $W_S/2\pi \simeq 20$ MHz in the tilted system. Subsequently, as W_S continues to increase, the decay of z becomes slower. In contrast, for the disordered system, α consistently decreases with increasing disordered strength W . We note that the impact of the emergence of dipole-moment conservation with increasing the slope of linear potential on the spin transport, and its distinction from the transport in disordered systems remain unclear and deserve further theoretical studies.

Discussion

Based on the novel protocol for simulating the infinite-temperature spin transport using the Haar-random state [40], we have experimentally probed diffusive transport on a 24-qubit ladder-type programmable superconducting processor. Moreover, when the qubit ladder is subject to sufficiently strong disorder, we observe the signatures of subdiffusive transport, in accompany with the breakdown of ergodicity due to MBL.

It is worthwhile to emphasize that previous experimental studies of the Stark MBL mainly focus on the dynamics of imbalance [50, 59, 60]. Different from the disorder-induced MBL with a power-law decay of imbalance observed in the subdiffusive Griffith-like region [61], for the Stark MBL, there is no experimental evidence for the power-law decay of imbalance [50, 59, 60]. Here, by measuring the infinite-temperature autocorrelation function, we provide solid experimental evidence for the subdiffusion in tilted systems, which is induced by the emergence of strong Hilbert-space fragmentation [55–57]. Theoretically, it has been suggested that for a thermodynamically large system, non-zero tilted potentials, i.e., $\Delta > 0$, will lead to a subdiffusive transport with $\alpha \simeq 1/4$ [17, 62]. In finite-size systems, both results as shown in Fig. 4 and the cold atom experiments on the tilted Fermi-Hubbard model [63] demonstrate a crossover from the diffusive regime to the subdiffusive one. Investigating how this crossover scales with an increasing system size is a further experimental task, which requires for quantum simulators with a larger number of qubits.

Ensembles of Haar-random pure quantum states have several promising applications, including benchmarking

quantum devices [42, 64] and demonstrating the beyond-classical computation [35–39]. Our work displays a practical application of the randomly distributed quantum state, i.e., probing the infinite-temperature spin transport. In contrast to employing digital random circuits, where the number of imperfect two-qubit gates is proportional to the qubit number [36–41], the scalable analog circuit adopted in our experiments can also generate multi-qubit Haar-random states useful for simulating hydrodynamics. The protocol employed in our work can be naturally extended to explore the non-trivial transport properties on other analog quantum simulators, including the Rydberg atoms [42, 65–67], quantum gas microscopes [68, 69], and the superconducting circuits with a central resonance bus, which enables long-range interactions [21, 70, 71].

Methods

Derivation of Eq. (4)

Here, we present the details of the deviation of Eq. (4), which is based on the typicality [12, 40, 72]. According to Eq. (2), $c_{\mu;\nu} = \text{Tr}[\hat{\sigma}_\mu^z(t)\hat{\sigma}_\nu^z]/D$, with $D = 2^N$. We define $\hat{N}_\nu = (\hat{\sigma}_\nu^z + 1)/2$, and then $c_{\mu;\nu} = \frac{1}{D} \text{Tr}[\hat{\sigma}_\mu^z(t)\hat{N}_\nu]$. By using $\hat{N}_\nu = (\hat{N}_\nu)^2$, we have $c_{\mu;\nu} = \frac{1}{D} \text{Tr}[\hat{N}_\nu\hat{\sigma}_\mu^z(t)\hat{N}_\nu]$. We note that \hat{N}_ν is an operator which projects the state of the ν -th qubit to the state $|0\rangle$.

According to the typicality [12, 40, 72], the trace of an operator \hat{O} can be approximated as the expectation value averaged by the pure Haar-random state $|r\rangle$, i.e.,

$$\frac{1}{D} \text{Tr}[\hat{O}] = \langle r|\hat{O}|r\rangle + \mathcal{O}(2^{-N/2}), \quad (5)$$

with N being the number of qubits. It indicates that the infinite-temperature expectation value $\text{Tr}[\hat{O}]/D$ can be better estimated by the expectation value for the Haar-random state $\langle r|\hat{O}|r\rangle$. Thus, $c_{\mu;\nu} \simeq \langle r|\hat{N}_\nu\hat{\sigma}_\mu^z(t)\hat{N}_\nu|r\rangle = \langle \psi_\nu^R(t)|\hat{\sigma}_\mu^z|\psi_\nu^R(t)\rangle$ for multi-qubit systems. Based on the definition of the projector \hat{N}_ν , $\hat{N}_\nu|r\rangle$ is a Haar-random state for the whole system except for the ν -th qubit, and in the experiment, only a $(N-1)$ -qubit Haar-random state is required.

Numerical simulations

Here, we present the details of the numerical simulations. We calculate the unitary time evolution $|\psi(t + \Delta t)\rangle = e^{-i\hat{H}\Delta t}|\psi(t)\rangle$ by employing the Krylov method [49]. The Krylov subspace is panned by the vectors defined as $\{|\psi(t)\rangle, \hat{H}|\psi(t)\rangle, \hat{H}^2|\psi(t)\rangle, \dots, \hat{H}^{(m-1)}|\psi(t)\rangle\}$. Then, the Hamiltonian \hat{H} in the Krylov subspace becomes a m -dimensional matrix $H_m = K_m^\dagger H K_m$, where H denotes the Hamiltonian \hat{H} in the matrix form, and K_m is the

matrix whose columns contain the orthonormal basis vectors of the Krylov space. Finally, the unitary time evolution can be approximately simulated in the Krylov subspace as $|\psi(t + \Delta t)\rangle \simeq \mathbf{K}_m^\dagger e^{-iH_m \Delta t} \mathbf{K}_m |\psi(t)\rangle$. In our numerical simulations, the dimension of the Krylov subspace m is adaptively adjusted from $m = 6$ to 30, making sure the numerical errors are smaller than 10^{-14} .

For the numerical simulation of the $\hat{U}_R(t_R) = e^{-i\hat{H}at_R}$ in Fig. 1c, based on the experimental data of the XY drive, the parameters in \hat{H}_d are $\Omega_{j,m}/2\pi = 10.4 \pm 1.6$ MHz, and $\phi_{j,m} \in [-\pi/10, \pi/10]$.

Details of generating Haar-random states

In this section, we present more details for the generation of faithful Haar-random states. The analog quantum circuit employed to generate Haar-random states is $\hat{U}_R = \exp[-i(\hat{H}_I + \hat{H}_d)t]$, where \hat{H}_I is given by Eq. (1) and $\hat{H}_d = \sum_{m \in \{\uparrow, \downarrow\}} \sum_{j=1}^L \Omega_{j,m} (e^{-i\phi_{j,m}} \hat{\sigma}_{j,m}^+ + e^{i\phi_{j,m}} \hat{\sigma}_{j,m}^-) / 2$ is the drive Hamiltonian.

Here, we first numerically study the influence of the driving amplitude $\Omega_{j,m}$. For convenience, we consider $\phi_{j,m} = 0$ and isotropic driving amplitude,

i.e., $\Omega = \Omega_{j,m}$ for all (j, m) . We chose $Q_R = \{Q_{1,\uparrow}, Q_{2,\uparrow}, \dots, Q_{12,\uparrow}, Q_{2,\downarrow}, Q_{3,\downarrow}, \dots, Q_{12,\downarrow}\}$ with total 23 qubits. The dynamics of participation entropy S_{PE} for different values of Ω are plotted in Fig. 5a, and the values of S_{PE} with the evolved time $t = 200$ ns and 1000 ns are displayed in Fig. 5b. It is seen that for small Ω , the growth of S_{PE} is slow and with increasing Ω , it becomes more rapid. In this experiment, we chose $\overline{\Omega}/\overline{J} \simeq 1.4$ because the participation entropy can achieve S_{PE}^{T} with a relatively short evolved time $t \simeq 200$ ns. As Ω further increases, the time when S_{PE}^{T} is reached does not significantly become shorter. Based on above discussions, $\overline{\Omega}/\overline{J} \simeq 1.4$ is an appropriate choice of the driving amplitude.

Next, we numerically study the influence of the randomness for the phases of driving microwave pulse $\phi_{j,m}$. In this experiment, by using the correction of crosstalk, the randomness of the phases is small, i.e., $\phi_{j,m} \in [-\pi/10, \pi/10]$. Here, we consider the phases with large randomness, i.e., $\phi_{j,m} \in [-\pi, \pi]$. The numerical results for the time evolution of S_{PE} with 5 samples of $\phi_{j,m}$ are plotted in Fig. 5c. With $\phi_{j,m} \in [-\pi, \pi]$, the participation entropy can still tend to S_{PE}^{T} around 200 ns. Only the short time behaviors are slightly different from each other for the 5 samples (see the inset of Fig. 5c).

-
- [1] R. Nandkishore and D. A. Huse, ‘‘Many-Body Localization and Thermalization in Quantum Statistical Mechanics,’’ *Annual Review of Condensed Matter Physics* **6**, 15–38 (2015).
 - [2] K. Agarwal, S. Gopalakrishnan, M. Knap, M. Muller, and E. Demler, ‘‘Anomalous Diffusion and Griffiths Effects Near the Many-Body Localization Transition,’’ *Phys. Rev. Lett.* **114**, 160401 (2015).
 - [3] M. ˙Znidaric, A. Scardicchio, and V. K. Varma, ‘‘Diffusive and Subdiffusive Spin Transport in the Ergodic Phase of a Many-Body Localizable System,’’ *Phys. Rev. Lett.* **117**, 040601 (2016).
 - [4] M. Ljubotina, J.-Y. Desaulles, M. Serbyn, and Z. Papic, ‘‘Superdiffusive Energy Transport in Kinetically Constrained Models,’’ *Phys. Rev. X* **13**, 011033 (2023).
 - [5] A. Scheie, N. E. Sherman, M. Dupont, S. E. Nagler, M. B. Stone, G. E. Granroth, J. E. Moore, and D. A. Tennant, ‘‘Detection of Kardar–Parisi–Zhang hydrodynamics in a quantum Heisenberg spin-1/2 chain,’’ *Nature Physics* **17**, 726–730 (2021).
 - [6] M. ˙Znidaric, ‘‘Spin Transport in a One-Dimensional Anisotropic Heisenberg Model,’’ *Phys. Rev. Lett.* **106**, 220601 (2011).
 - [7] M. Dupont, N. E. Sherman, and J. E. Moore, ‘‘Spatiotemporal Crossover between Low- and High-Temperature Dynamical Regimes in the Quantum Heisenberg Magnet,’’ *Phys. Rev. Lett.* **127**, 107201 (2021).
 - [8] B. Bertini, F. Heidrich-Meisner, C. Karrasch, T. Prosen, R. Steinigeweg, and M. ˙Znidaric, ‘‘Finite-temperature transport in one-dimensional quantum lattice models,’’ *Rev. Mod. Phys.* **93**, 025003 (2021).
 - [9] J. Eisert, M. Friesdorf, and C. Gogolin, ‘‘Quantum many-body systems out of equilibrium,’’ *Nature Physics* **11**, 124–130 (2015).
 - [10] P. Peng, B. Ye, N. Y. Yao, and P. Cappellaro, ‘‘Exploiting disorder to probe spin and energy hydrodynamics,’’ *Nature Physics* (2023).
 - [11] R. Steinigeweg, F. Heidrich-Meisner, J. Gemmer, K. Michielsen, and H. De Raedt, ‘‘Scaling of diffusion constants in the spin- $\frac{1}{2}$ XX ladder,’’ *Phys. Rev. B* **90**, 094417 (2014).
 - [12] D. Schubert, J. Richter, F. Jin, K. Michielsen, H. De Raedt, and R. Steinigeweg, ‘‘Quantum versus classical dynamics in spin models: Chains, ladders, and square lattices,’’ *Phys. Rev. B* **104**, 054415 (2021).
 - [13] Marko Ljubotina, Marko ˙Znidaric, and Toma ˙z Prosen, ‘‘Spin diffusion from an inhomogeneous quench in an integrable system,’’ *Nature Communications* **8**, 16117 (2017).
 - [14] David Wei, Antonio Rubio-Abadal, Bingtian Ye, Francisco Machado, Jack Kemp, Kritsana Srakaew, Simon Hollerith, Jun Rui, Sarang Gopalakrishnan, Norman Y. Yao, Immanuel Bloch, and Johannes Zeiher, ‘‘Quantum gas microscopy of Kardar-Parisi-Zhang superdiffusion,’’ *Science* **376**, 716–720 (2022).

- [15] M. K. Joshi, F. Kranzl, A. Schuckert, I. Lovas, C. Maier, R. Blatt, M. Knap, and C. F. Roos, “Observing emergent hydrodynamics in a long-range quantum magnet,” *Science* **376**, 720–724 (2022).
- [16] E. Rosenberg, T. I. Andersen, R. Samajdar, A. Petukhov, J. C. Hoke, D. Abanin, A. Bengtsson, I. K. Drozdov, C. Erickson, P. V. Klimov, X. Mi, A. Morvan, M. Neeley, C. Neill, R. Acharya, R. Allen, K. Anderson, M. Ansmann, F. Arute, K. Arya, A. Asfaw, J. Atalaya, J. C. Bardin, A. Bilmes, G. Bortoli, A. Bourassa, J. Bovaird, L. Brill, M. Broughton, B. B. Buckley, D. A. Buell, T. Burger, B. Burkett, N. Bushnell, J. Campero, H.-S. Chang, Z. Chen, B. Chiaro, D. Chik, J. Cogan, R. Collins, P. Conner, W. Courtney, A. L. Crook, B. Curtin, D. M. Debroy, A. Del Toro Barba, S. Demura, A. Di Paolo, A. Dunsworth, C. Earle, L. Faoro, E. Farhi, R. Fatemi, V. S. Ferreira, L. Flores Burgos, E. Forati, A. G. Fowler, B. Foxen, G. Garcia, É. Genois, W. Jiang, C. Gidney, D. Gilboa, M. Giustina, R. Gosula, A. Grajales Dau, J. A. Gross, S. Habegger, M. C. Hamilton, M. Hansen, M. P. Harrigan, S. D. Harrington, P. Heu, G. Hill, M. R. Hoffmann, S. Hong, T. Huang, A. Huff, W. J. Huggins, L. B. Ioffe, S. V. Isakov, J. Iveland, E. Jeffrey, Z. Jiang, C. Jones, P. Juhás, D. Kafri, T. Khattar, M. Khezri, M. Kieferová, S. Kim, A. Kitaev, A. R. Klots, A. N. Korotkov, F. Kostritsa, J. M. Kreikebaum, D. Landhuis, P. Laptev, K.-M. Lau, L. Laws, J. Lee, K. W. Lee, Y. D. Lensky, B. J. Lester, A. T. Lill, W. Liu, A. Locharla, S. Mandrà, O. Martin, S. Martin, J. R. McClean, M. McEwen, S. Meeks, K. C. Miao, A. Mieszala, S. Montazeri, R. Movassagh, W. Mruczkiewicz, A. Nersisyan, M. Newman, J. H. Ng, A. Nguyen, M. Nguyen, M. Y. Niu, T. E. O’Brien, S. Omonije, A. Opremcak, R. Potter, L. P. Pryadko, C. Quintana, D. M. Rhodes, C. Rocque, N. C. Rubin, N. Saei, D. Sank, K. Sankaragomathi, K. J. Satzinger, H. F. Schurkus, C. Schuster, M. J. Shearn, A. Shorter, N. Shutty, V. Shvarts, V. Sivak, J. Skrzynny, W. Clarke Smith, R. D. Somma, G. Sterling, D. Strain, M. Szalay, D. Thor, A. Torres, G. Vidal, B. Villalonga, C. Vollgraft Heidweiller, T. White, B. W. K. Woo, C. Xing, Z. Jamie Yao, P. Yeh, J. Yoo, G. Young, A. Zalcman, Y. Zhang, N. Zhu, N. Zobrist, H. Neven, R. Babbush, D. Bacon, S. Boixo, J. Hilton, E. Lucero, A. Megrant, J. Kelly, Y. Chen, V. Smelyanskiy, V. Khemani, S. Gopalakrishnan, T. Prosen, and P. Roushan, “Dynamics of magnetization at infinite temperature in a Heisenberg spin chain,” *Science* **384**, 48–53 (2024).
- [17] J. Feldmeier, P. Sala, G. De Tomasi, F. Pollmann, and M. Knap, “Anomalous diffusion in dipole- and higher-moment-conserving systems,” *Phys. Rev. Lett.* **125**, 245303 (2020).
- [18] J. De Nardis, S. Gopalakrishnan, R. Vasseur, and B. Ware, “Subdiffusive hydrodynamics of nearly integrable anisotropic spin chains,” *Proceedings of the National Academy of Sciences* **119**, e2202823119 (2022).
- [19] A. Gromov, A. Lucas, and R. M. Nandkishore, “Fracton hydrodynamics,” *Phys. Rev. Res.* **2**, 033124 (2020).
- [20] Ruichao Ma, Brendan Saxberg, Clai Owens, Nelson Leung, Yao Lu, Jonathan Simon, and David I. Schuster, “A dissipatively stabilized Mott insulator of photons,” *Nature* **566**, 51–57 (2019).
- [21] X. Zhang, E. Kim, D. K. Mark, S. Choi, and O. Painter, “A superconducting quantum simulator based on a photonic-bandgap metamaterial,” *Science* **379**, 278–283 (2023).
- [22] Zhong-Cheng Xiang, Kaixuan Huang, Yu-Ran Zhang, Tao Liu, Yun-Hao Shi, Cheng-Lin Deng, Tong Liu, Hao Li, Gui-Han Liang, Zheng-Yang Mei, Haifeng Yu, Guangming Xue, Ye Tian, Xiaohui Song, Zhi-Bo Liu, Kai Xu, Dongning Zheng, Franco Nori, and Heng Fan, “Simulating Chern insulators on a superconducting quantum processor,” *Nature Communications* **14**, 5433 (2023).
- [23] Xiu Gu, Anton Frisk Kockum, Adam Miranowicz, Yu-xi Liu, and Franco Nori, “Microwave photonics with superconducting quantum circuits,” *Physics Reports* **718-719**, 1–102 (2017).
- [24] Fusheng Chen, Zheng-Hang Sun, Ming Gong, Qingling Zhu, Yu-Ran Zhang, Yulin Wu, Yangsen Ye, Chen Zha, Shaowei Li, Shaojun Guo, Haoran Qian, He-Liang Huang, Jiale Yu, Hui Deng, Hao Rong, Jin Lin, Yu Xu, Lihua Sun, Cheng Guo, Na Li, Futian Liang, Cheng-Zhi Peng, Heng Fan, Xiaobo Zhu, and Jian-Wei Pan, “Observation of Strong and Weak Thermalization in a Superconducting Quantum Processor,” *Phys. Rev. Lett.* **127**, 020602 (2021).
- [25] Qingling Zhu, Zheng-Hang Sun, Ming Gong, Fusheng Chen, Yu-Ran Zhang, Yulin Wu, Yangsen Ye, Chen Zha, Shaowei Li, Shaojun Guo, Haoran Qian, He-Liang Huang, Jiale Yu, Hui Deng, Hao Rong, Jin Lin, Yu Xu, Lihua Sun, Cheng Guo, Na Li, Futian Liang, Cheng-Zhi Peng, Heng Fan, Xiaobo Zhu, and Jian-Wei Pan, “Observation of Thermalization and Information Scrambling in a Superconducting Quantum Processor,” *Phys. Rev. Lett.* **128**, 160502 (2022).
- [26] P. Roushan, C. Neill, J. Tangpanitanon, V. M. Bastidas, A. Megrant, R. Barends, Y. Chen, Z. Chen, B. Chiaro, A. Dunsworth, A. Fowler, B. Foxen, M. Giustina, E. Jeffrey, J. Kelly, E. Lucero, J. Mutus, M. Neeley, C. Quintana, D. Sank, A. Vainsencher, J. Wenner, T. White, H. Neven, D. G. Angelakis, and J. Martinis, “Spectroscopic signatures of localization with interacting photons in superconducting qubits,” *Science* **358**, 1175–1179 (2017).
- [27] Qiujiang Guo, Chen Cheng, Zheng-Hang Sun, Zixuan Song, Hekang Li, Zhen Wang, Wenhui Ren, Hang Dong, Dongning Zheng, Yu-Ran Zhang, Rubem Mondaini, Heng Fan, and H. Wang, “Observation of energy-resolved many-body localization,” *Nature Physics* **17**, 234–239 (2021).
- [28] Qiujiang Guo, Chen Cheng, Hekang Li, Shibo Xu, Pengfei Zhang, Zhen Wang, Chao Song, Wuxin Liu, Wenhui Ren, Hang Dong, Rubem Mondaini, and H. Wang, “Stark Many-Body Localization on a Superconducting Quantum Processor,” *Phys. Rev. Lett.* **127**, 240502 (2021).
- [29] Pengfei Zhang, Hang Dong, Yu Gao, Liangtian Zhao, Jie Hao, Jean-Yves Desautels, Qiujiang Guo, Jiachen Chen, Jinfeng Deng, Bobo Liu, Wenhui Ren, Yunyan Yao, Xu Zhang, Shibo Xu, Ke Wang, Feitong Jin, Xuhao Zhu, Bing Zhang, Hekang Li, Chao Song, Zhen Wang, Fangli

- Liu, Zlatko Papić, Lei Ying, H. Wang, and Ying-Cheng Lai, “Many-body Hilbert space scarring on a superconducting processor,” *Nature Physics* **19**, 120–125 (2023).
- [30] Xu Zhang, Wenjie Jiang, Jinfeng Deng, Ke Wang, Jiachen Chen, Pengfei Zhang, Wenhui Ren, Hang Dong, Shibo Xu, Yu Gao, Feitong Jin, Xuhao Zhu, Qiujiang Guo, Hekang Li, Chao Song, Alexey V. Gorshkov, Thomas Iadecola, Fangli Liu, Zhe-Xuan Gong, Zhen Wang, Dong-Ling Deng, and H. Wang, “Digital quantum simulation of Floquet symmetry-protected topological phases,” *Nature* **607**, 468–473 (2022).
- [31] Xiao Mi, Matteo Ippoliti, Chris Quintana, Ami Greene, Zijun Chen, Jonathan Gross, Frank Arute, Kunal Arya, Juan Atalaya, Ryan Babbush, Joseph C. Bardin, Joao Basso, Andreas Bengtsson, Alexander Bilmes, Alexandre Bourassa, Leon Brill, Michael Broughton, Bob B. Buckley, David A. Buell, Brian Burkett, Nicholas Bushnell, Benjamin Chiaro, Roberto Collins, William Courtney, Dripto Debroy, Sean Demura, Alan R. Derk, Andrew Dunsworth, Daniel Eppens, Catherine Erickson, Edward Farhi, Austin G. Fowler, Brooks Foxen, Craig Gidney, Marissa Giustina, Matthew P. Harrigan, Sean D. Harrington, Jeremy Hilton, Alan Ho, Sabrina Hong, Trent Huang, Ashley Huff, William J. Huggins, L. B. Ioffe, Sergei V. Isakov, Justin Iveland, Evan Jeffrey, Zhang Jiang, Cody Jones, Dvir Kafri, Tanuj Khattar, Seon Kim, Alexei Kitaev, Paul V. Klimov, Alexander N. Korotkov, Fedor Kostritsa, David Landhuis, Pavel Laptev, Joonho Lee, Kenny Lee, Aditya Locharla, Erik Lucero, Orion Martin, Jarrod R. McClean, Trevor McCourt, Matt McEwen, Kevin C. Miao, Masoud Mohseni, Shirin Montazeri, Wojciech Mroczkiewicz, Ofer Naaman, Matthew Neeley, Charles Neill, Michael Newman, Murphy Yuezhen Niu, Thomas E. O’Brien, Alex Opremcak, Eric Ostby, Balint Pato, Andre Petukhov, Nicholas C. Rubin, Daniel Sank, Kevin J. Satzinger, Vladimir Shvarts, Yuan Su, Doug Strain, Marco Szalay, Matthew D. Trevithick, Benjamin Villalonga, Theodore White, Z. Jamie Yao, Ping Yeh, Juhwan Yoo, Adam Zalcman, Hartmut Neven, Sergio Boixo, Vadim Smelyanskiy, Anthony Megrant, Julian Kelly, Yu Chen, S. L. Sondhi, Roderich Moessner, Kostyantyn Kechedzhi, Vedika Khemani, and Pedram Roushan, “Time-crystalline eigenstate order on a quantum processor,” *Nature* **601**, 531–536 (2022).
- [32] P. Frey and S. Rachel, “Realization of a discrete time crystal on 57 qubits of a quantum computer,” *Science Advances* **8**, eabm7652 (2022).
- [33] Xiao Mi, Pedram Roushan, Chris Quintana, Salvatore Mandrà, Jeffrey Marshall, Charles Neill, Frank Arute, Kunal Arya, Juan Atalaya, Ryan Babbush, Joseph C. Bardin, Rami Barends, Joao Basso, Andreas Bengtsson, Sergio Boixo, Alexandre Bourassa, Michael Broughton, Bob B. Buckley, David A. Buell, Brian Burkett, Nicholas Bushnell, Zijun Chen, Benjamin Chiaro, Roberto Collins, William Courtney, Sean Demura, Alan R. Derk, Andrew Dunsworth, Daniel Eppens, Catherine Erickson, Edward Farhi, Austin G. Fowler, Brooks Foxen, Craig Gidney, Marissa Giustina, Jonathan A. Gross, Matthew P. Harrigan, Sean D. Harrington, Jeremy Hilton, Alan Ho, Sabrina Hong, Trent Huang, William J. Huggins, L. B. Ioffe, Sergei V. Isakov, Evan Jeffrey, Zhang Jiang, Cody Jones, Dvir Kafri, Julian Kelly, Seon Kim, Alexei Kitaev, Paul V. Klimov, Alexander N. Korotkov, Fedor Kostritsa, David Landhuis, Pavel Laptev, Erik Lucero, Orion Martin, Jarrod R. McClean, Trevor McCourt, Matt McEwen, Anthony Megrant, Kevin C. Miao, Masoud Mohseni, Shirin Montazeri, Wojciech Mroczkiewicz, Josh Mutus, Ofer Naaman, Matthew Neeley, Michael Newman, Murphy Yuezhen Niu, Thomas E. O’Brien, Alex Opremcak, Eric Ostby, Balint Pato, Andre Petukhov, Nicholas Redd, Nicholas C. Rubin, Daniel Sank, Kevin J. Satzinger, Vladimir Shvarts, Doug Strain, Marco Szalay, Matthew D. Trevithick, Benjamin Villalonga, Theodore White, Z. Jamie Yao, Ping Yeh, Adam Zalcman, Hartmut Neven, Hartmut Neven, Igor Aleiner, Kostyantyn Kechedzhi, Vadim Smelyanskiy, and Yu Chen, “Information scrambling in quantum circuits,” *Science* **374**, 1479–1483 (2021).
- [34] Jochen Braumüller, Amir H. Karamlou, Yariv Yanay, Bharath Kannan, David Kim, Morten Kjaergaard, Alexander Melville, Bethany M. Niedzielski, Youngkyu Sung, Antti Vepsäläinen, Roni Winik, Jonilyn L. Yoder, Terry P. Orlando, Simon Gustavsson, Charles Tahan, and William D. Oliver, “Probing quantum information propagation with out-of-time-ordered correlators,” *Nature Physics* **18**, 172–178 (2022).
- [35] C. Neill, P. Roushan, K. Kechedzhi, S. Boixo, S. V. Isakov, V. Smelyanskiy, A. Megrant, B. Chiaro, A. Dunsworth, K. Arya, R. Barends, B. Burkett, Y. Chen, Z. Chen, A. Fowler, B. Foxen, M. Giustina, R. Graff, E. Jeffrey, T. Huang, J. Kelly, P. Klimov, E. Lucero, J. Mutus, M. Neeley, C. Quintana, D. Sank, A. Vainsencher, J. Wenner, T. C. White, H. Neven, and J. M. Martinis, “A blueprint for demonstrating quantum supremacy with superconducting qubits,” *Science* **360**, 195–199 (2018).
- [36] Sergio Boixo, Sergei V. Isakov, Vadim N. Smelyanskiy, Ryan Babbush, Nan Ding, Zhang Jiang, Michael J. Bremner, John M. Martinis, and Hartmut Neven, “Characterizing quantum supremacy in near-term devices,” *Nature Physics* **14**, 595–600 (2018).
- [37] F. Arute *et al.*, “Quantum supremacy using a programmable superconducting processor,” *Nature* **574**, 505–510 (2019).
- [38] Yulin Wu, Wan-Su Bao, Sirui Cao, Fusheng Chen, Ming-Cheng Chen, Xiawei Chen, Tung-Hsun Chung, Hui Deng, Yajie Du, Daojin Fan, Ming Gong, Cheng Guo, Chu Guo, Shaojun Guo, Lianchen Han, Linyin Hong, He-Liang Huang, Yong-Heng Huo, Liping Li, Na Li, Shaowei Li, Yuan Li, Futian Liang, Chun Lin, Jin Lin, Hao-ran Qian, Dan Qiao, Hao Rong, Hong Su, Lihua Sun, Liangyuan Wang, Shiyu Wang, Dachao Wu, Yu Xu, Kai Yan, Weifeng Yang, Yang Yang, Yangsen Ye, Jianghan Yin, Chong Ying, Jiale Yu, Chen Zha, Cha Zhang, Haibin Zhang, Kaili Zhang, Yiming Zhang, Han Zhao, Youwei Zhao, Liang Zhou, Qingling Zhu, Chao-Yang Lu, Cheng-Zhi Peng, Xiaobo Zhu, and Jian-Wei Pan, “Strong Quantum Computational Advantage Using a Superconducting Quantum Processor,” *Phys. Rev. Lett.* **127**, 180501 (2021).
- [39] A. Morvan, B. Villalonga, X. Mi, S. Mandrà, A. Bengts-

- son, P. V. Klimov, Z. Chen, S. Hong, C. Erickson, I. K. Drozdov, J. Chau, G. Laun, R. Movassagh, A. Asfaw, L. T. A. N. Brandão, R. Peralta, D. Abanin, R. Acharya, R. Allen, T. I. Andersen, K. Anderson, M. Ansmann, F. Arute, K. Arya, J. Atalaya, J. C. Bardin, A. Bilmes, G. Bortoli, A. Bourassa, J. Bovaird, L. Brill, M. Broughton, B. B. Buckley, D. A. Buell, T. Burger, B. Burkett, N. Bushnell, J. Campero, H. S. Chang, B. Chiaro, D. Chik, C. Chou, J. Cogan, R. Collins, P. Conner, W. Courtney, A. L. Crook, B. Curtin, D. M. Debroy, A. Del Toro Barba, S. Demura, A. Di Paolo, A. Dunsworth, L. Faoro, E. Farhi, R. Fatemi, V. S. Ferreira, L. Flores Burgos, E. Forati, A. G. Fowler, B. Foxen, G. Garcia, E. Genois, W. Giang, C. Gidney, D. Gilboa, M. Giustina, R. Gosula, A. Grajales Dau, J. A. Gross, S. Habegger, M. C. Hamilton, M. Hansen, M. P. Harrigan, S. D. Harrington, P. Heu, M. R. Hoffmann, T. Huang, A. Huff, W. J. Huggins, L. B. Ioffe, S. V. Isakov, J. Iveland, E. Jeffrey, Z. Jiang, C. Jones, P. Juhas, D. Kafri, T. Khattar, M. Khezri, M. Kieferová, S. Kim, A. Kitaev, A. R. Klots, A. N. Korotkov, F. Kostritsa, J. M. Kreikebaum, D. Landhuis, P. Laptev, K. M. Lau, L. Laws, J. Lee, K. W. Lee, Y. D. Lensky, B. J. Lester, A. T. Lill, W. Liu, W. P. Livingston, A. Locharla, F. D. Malone, O. Martin, S. Martin, J. R. McClean, M. McEwen, K. C. Miao, A. Mieszala, S. Montazeri, W. Mruczkiewicz, O. Naaman, M. Neeley, C. Neill, A. Nersisyan, M. Newman, J. H. Ng, A. Nguyen, M. Nguyen, M. Yuezhen Niu, T. E. O'Brien, S. Omonije, A. Opremcak, A. Petukhov, R. Potter, L. P. Pryadko, C. Quintana, D. M. Rhodes, E. Rosenberg, C. Rocque, P. Roushan, N. C. Rubin, N. Saei, D. Sank, K. Sankaragomathi, K. J. Satzinger, H. F. Schurkus, C. Schuster, M. J. Shearn, A. Shorter, N. Shutty, V. Shvarts, V. Sivak, J. Skrzynny, W. C. Smith, R. D. Somma, G. Sterling, D. Strain, M. Szalay, D. Thor, A. Torres, G. Vidal, C. Vollgraff Heidweiller, T. White, B. W. K. Woo, C. Xing, Z. J. Yao, P. Yeh, J. Yoo, G. Young, A. Zalcman, Y. Zhang, N. Zhu, N. Zobrist, E. G. Rieffel, R. Biswas, R. Babbush, D. Bacon, J. Hilton, E. Lucero, H. Neven, A. Megrant, J. Kelly, I. Aleiner, V. Smelyanskiy, K. Kechedzhi, Y. Chen, and S. Boixo, "Phase transition in Random Circuit Sampling," (2023), [arXiv:2304.11119](https://arxiv.org/abs/2304.11119).
- [40] J. Richter and A. Pal, "Simulating hydrodynamics on noisy intermediate-scale quantum devices with random circuits," *Phys. Rev. Lett.* **126**, 230501 (2021).
- [41] N. Keenan, N. F. Robertson, T. Murphy, S. Zhuk, and J. Goold, "Evidence of Kardar-Parisi-Zhang scaling on a digital quantum simulator," *npj Quantum Information* **9**, 72 (2023).
- [42] Joonhee Choi, Adam L. Shaw, Ivaylo S. Madjarov, Xin Xie, Ran Finkelstein, Jacob P. Covey, Jordan S. Cotler, Daniel K. Mark, Hsin-Yuan Huang, Anant Kale, Hannes Pichler, Fernando G. S. L. Brandão, Soonwon Choi, and Manuel Endres, "Preparing random states and benchmarking with many-body quantum chaos," *Nature* **613**, 468–473 (2023).
- [43] Amir H. Karamlou, Ilan T. Rosen, Sarah E. Muschinske, Cora N. Barrett, Agustin Di Paolo, Leon Ding, Patrick M. Harrington, Max Hays, Rabindra Das, David K. Kim, Bethany M. Niedzielski, Meghan Schuldt, Kyle Serniak, Mollie E. Schwartz, Jonilyn L. Yoder, Simon Gustavsson, Yariv Yanay, Jeffrey A. Grover, and William D. Oliver, "Probing entanglement in a 2D hard-core Bose–Hubbard lattice," *Nature* **629**, 561–566 (2024).
- [44] Yariv Yanay, Jochen Braumüller, Simon Gustavsson, William D. Oliver, and Charles Tahan, "Two-dimensional hard-core Bose–Hubbard model with superconducting qubits," *npj Quantum Information* **6**, 58 (2020).
- [45] Z.-H. Sun, J. Cui, and H. Fan, "Characterizing the many-body localization transition by the dynamics of diagonal entropy," *Phys. Rev. Res.* **2**, 013163 (2020).
- [46] I. Khait, S. Gazit, N. Y. Yao, and A. Auerbach, "Spin transport of weakly disordered heisenberg chain at infinite temperature," *Phys. Rev. B* **93**, 224205 (2016).
- [47] S. Gopalakrishnan, K. Agarwal, E. A. Demler, D. A. Huse, and M. Knap, "Griffiths effects and slow dynamics in nearly many-body localized systems," *Phys. Rev. B* **93**, 134206 (2016).
- [48] F. Setiawan, D.-L. Deng, and J. H. Pixley, "Transport properties across the many-body localization transition in quasiperiodic and random systems," *Phys. Rev. B* **96**, 104205 (2017).
- [49] D. J. Luitz and Y. B. Lev, "The ergodic side of the many-body localization transition," *Annalen der Physik* **529**, 1600350 (2017).
- [50] W. Morong, F. Liu, P. Becker, K. S. Collins, L. Feng, A. Kyprianidis, G. Pagano, T. You, A. V. Gorshkov, and C. Monroe, "Observation of Stark many-body localization without disorder," *Nature* **599**, 393–398 (2021).
- [51] M. Schulz, C. A. Hooley, R. Moessner, and F. Pollmann, "Stark Many-Body Localization," *Phys. Rev. Lett.* **122**, 040606 (2019).
- [52] E. van Nieuwenburg, Y. Baum, and G. Refael, "From Bloch oscillations to many-body localization in clean interacting systems," *Proceedings of the National Academy of Sciences* **116**, 9269–9274 (2019).
- [53] Y.-Y. Wang, Z.-H. Sun, and H. Fan, "Stark many-body localization transitions in superconducting circuits," *Phys. Rev. B* **104**, 205122 (2021).
- [54] S. R. Taylor, M. Schulz, F. Pollmann, and R. Moessner, "Experimental probes of Stark many-body localization," *Phys. Rev. B* **102**, 054206 (2020).
- [55] E. V. H. Doggen, I. V. Gornyi, and D. G. Polyakov, "Stark many-body localization: Evidence for Hilbert-space shattering," *Phys. Rev. B* **103**, L100202 (2021).
- [56] V. Khemani, M. Hermele, and R. Nandkishore, "Localization from Hilbert space shattering: From theory to physical realizations," *Phys. Rev. B* **101**, 174204 (2020).
- [57] P. Sala, T. Rakovszky, R. Verresen, M. Knap, and F. Pollmann, "Ergodicity breaking arising from Hilbert space fragmentation in dipole-conserving Hamiltonians," *Phys. Rev. X* **10**, 011047 (2020).
- [58] Maksym Serbyn, Z. Papić, and Dmitry A. Abanin, "Local Conservation Laws and the Structure of the Many-Body Localized States," *Phys. Rev. Lett.* **111**, 127201 (2013).
- [59] Sebastian Scherg, Thomas Kohlert, Pablo Sala, Frank Pollmann, Bharath Hebbe Madhusudhana, Immanuel

- Bloch, and Monika Aidelsburger, “Observing non-ergodicity due to kinetic constraints in tilted Fermi-Hubbard chains,” *Nature Communications* **12**, 4490 (2021).
- [60] Thomas Kohlert, Sebastian Scherg, Pablo Sala, Frank Pollmann, Bharath Hebhe Madhusudhana, Immanuel Bloch, and Monika Aidelsburger, “Exploring the regime of fragmentation in strongly tilted fermi-hubbard chains,” *Phys. Rev. Lett.* **130**, 010201 (2023).
- [61] Pranjal Bordia, Henrik Lüschen, Sebastian Scherg, Sarang Gopalakrishnan, Michael Knap, Ulrich Schneider, and Immanuel Bloch, “Probing Slow Relaxation and Many-Body Localization in Two-Dimensional Quasiperiodic Systems,” *Phys. Rev. X* **7**, 041047 (2017).
- [62] S. Nandy, J. Herbrych, Z. Lenarčič, A. Głódkowski, P. Prelovšek, and M. Mierzejewski, “Emergent dipole moment conservation and subdiffusion in tilted chains,” *Phys. Rev. B* **109**, 115120 (2024).
- [63] Elmer Guardado-Sanchez, Alan Morningstar, Benjamin M. Spar, Peter T. Brown, David A. Huse, and Waseem S. Bakr, “Subdiffusion and Heat Transport in a Tilted Two-Dimensional Fermi-Hubbard System,” *Phys. Rev. X* **10**, 011042 (2020).
- [64] A. W. Cross, L. S. Bishop, S. Sheldon, P. D. Nation, and J. M. Gambetta, “Validating quantum computers using randomized model circuits,” *Phys. Rev. A* **100**, 032328 (2019).
- [65] M. Saffman, T. G. Walker, and K. Mølmer, “Quantum information with rydberg atoms,” *Rev. Mod. Phys.* **82**, 2313–2363 (2010).
- [66] A. Browaeys and T. Lahaye, “Many-body physics with individually controlled rydberg atoms,” *Nature Physics* **16**, 132–142 (2020).
- [67] L. Henriot, L. Beguin, A. Signoles, T. Lahaye, A. Browaeys, G.-O. Raymond, and C. Jurczak, “Quantum computing with neutral atoms,” *Quantum* **4**, 327 (2020).
- [68] Adam M. Kaufman, M. Eric Tai, Alexander Lukin, Matthew Rispoli, Robert Schittko, Philipp M. Preiss, and Markus Greiner, “Quantum thermalization through entanglement in an isolated many-body system,” *Science* **353**, 794–800 (2016).
- [69] C. Gross and I. Bloch, “Quantum simulations with ultracold atoms in optical lattices,” *Science* **357**, 995–1001 (2017).
- [70] Kai Xu, Zheng-Hang Sun, Wuxin Liu, Yu-Ran Zhang, Hekang Li, Hang Dong, Wenhui Ren, Pengfei Zhang, Franco Nori, Dongning Zheng, Heng Fan, and H. Wang, “Probing dynamical phase transitions with a superconducting quantum simulator,” *Science Advances* **6** (2020), 10.1126/sciadv.aba4935.
- [71] Kai Xu, Yu-Ran Zhang, Zheng-Hang Sun, Hekang Li, Pengtao Song, Zhongcheng Xiang, Kaixuan Huang, Hao Li, Yun-Hao Shi, Chi-Tong Chen, Xiaohui Song, Dongning Zheng, Franco Nori, H. Wang, and Heng Fan, “Metrological Characterization of Non-Gaussian Entangled States of Superconducting Qubits,” *Phys. Rev. Lett.* **128**, 150501 (2022).
- [72] F. Jin, D. Willsch, M. Willsch, H. Lagemann, K. Michielsen, and H. De Raedt, “Random State Technol-

ogy,” *Journal of the Physical Society of Japan* **90**, 012001 (2020).

Data availability

The authors declare that the data supporting the findings of this study are available within the paper and its Supplementary Information files. Should any raw data files be needed in another format they are available from the corresponding author upon reasonable request. Source data are provided with this paper.

Acknowledgments

We thank Hai-Long Shi and H. S. Yan for helpful discussions. Z.X., D.Z., K.X. and H.F. are supported by Beijing Natural Science Foundation (Grant No. Z200009), National Natural Science Foundation of China (Grants Nos. 92265207, T2121001, 12122504, 12247168, 11934018, T2322030), Innovation Program for Quantum Science and Technology (Grant No. 2021ZD0301800), Beijing Nova Program (Nos. 20220484121, 2022000216). Y.-H.S. acknowledges the support of Postdoctoral Fellowship Program of CPSF (Grant No. GZB20240815). Z.-A.W. acknowledges the support of China Postdoctoral Science Foundation (Grant No. 2022TQ0036).

Author contributions

H.F. supervised the project. Z.-H.S. proposed the idea. Y.-H.S. conducted the experiment with the help of K.H. and K.X.. Z.-H.S., Y.-Y.W., and Y.-H.S. performed the numerical simulations. Z.X. and D.Z. fabricated the ladder-type sample. X.S., G.X., and H.Y. provided the Josephson parametric amplifiers. W.-G.M., H.-T.L., K.Z., J.-C.S., G.-H.L., Z.-Y.M., J.-C.Z., H.L., and C.-T.C. helped the experimental setup. Z.-A.W., Y.-R.Z., J.W., K.X., and H.F. discussed and commented on the manuscript. Z.-H.S., Y.-H.S., Y.-Y.W., Y.-R.Z., and H.F. co-wrote the manuscript. All authors contributed to the discussions of the results and development of the manuscript.

Competing interests

The authors declare no competing interests.

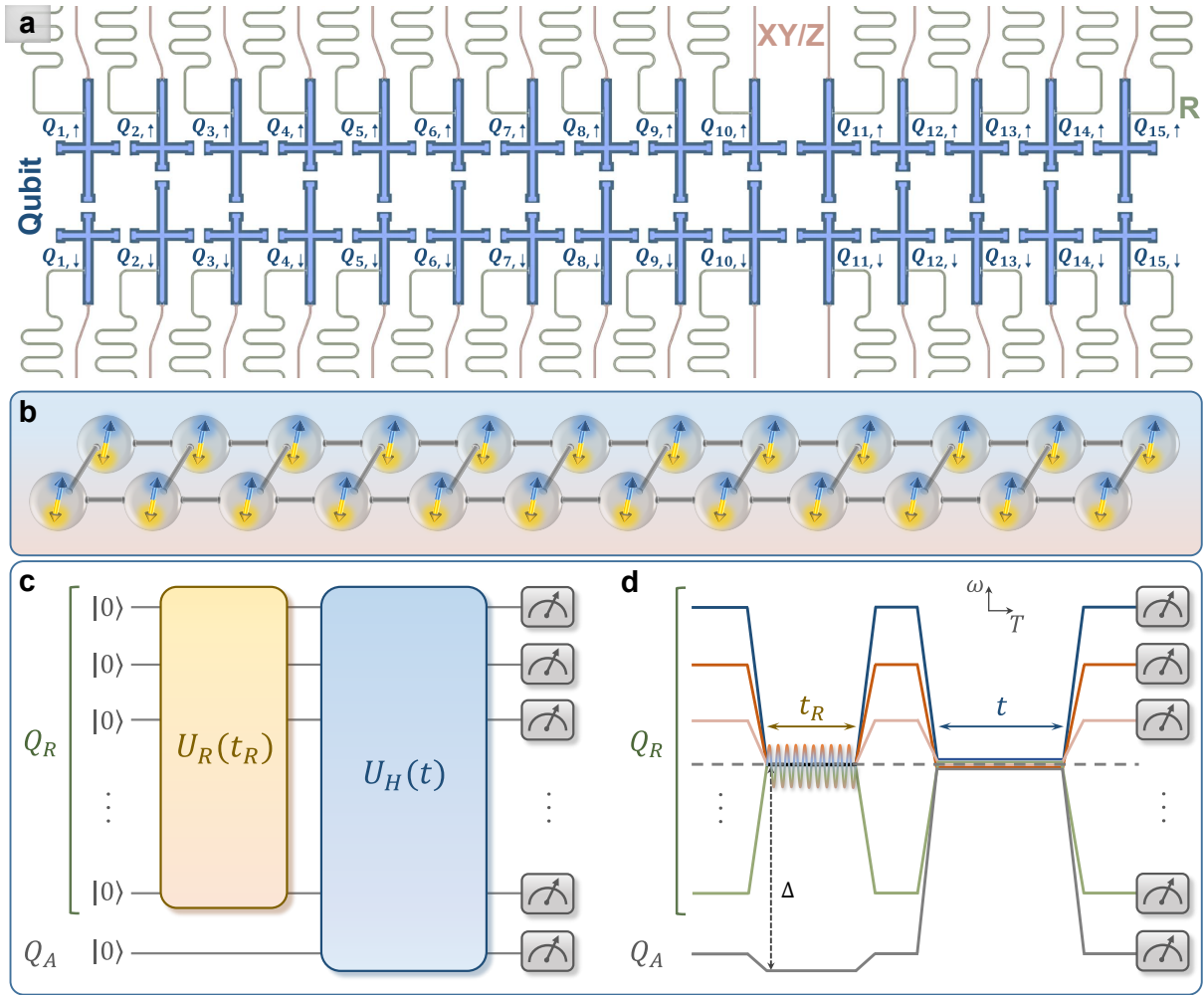


FIG. 1. **Superconducting quantum simulator and experimental pulse sequences.** **a**, The schematic showing the ladder-type superconducting quantum simulator, consisting of 30 qubits (the blue region), labeled $Q_{1,\uparrow}$ to $Q_{15,\uparrow}$, and $Q_{1,\downarrow}$ to $Q_{15,\downarrow}$. Each qubit is coupled to a separate readout resonator (the green region), and has an individual control line (the red region) for both the XY and Z controls. **b**, Schematic diagram of the simulated 24 spins coupled in a ladder. The blue and yellow double arrows represent the infinite-temperature spin hydrodynamics without preference for spin orientations. **c**, Schematic diagram of the quantum circuit for measuring the autocorrelation functions at infinite temperature. All qubits are initialized at the state $|0\rangle$. Subsequently, an analog quantum circuit $\hat{U}_R(t_R)$ acts on the set of qubits Q_R to generate Haar-random states. This is followed by a time evolution of all qubits, i.e., $\hat{U}_H(t) = \exp(-i\hat{H}t)$ with \hat{H} being the Hamiltonian of the system, in which the properties of spin transport are of our interest. **d**, Experimental pulse sequences corresponding to the quantum circuit in **c**, displayed in the frequency (ω) versus time (T) domain. To realize $\hat{U}_R(t_R)$, qubits in the set Q_R are tuned to the working point (dashed horizontal line) via Z pulses, and simultaneously, the resonant microwave pulses represented as the sinusoidal line are applied to Q_R through the XY control lines. Meanwhile, the qubit Q_A is detuned from the working point with a large value of the frequency gap Δ . To realize the subsequent evolution $\hat{U}_H(t)$ with the Hamiltonian (1), all qubits are tuned to the working point.

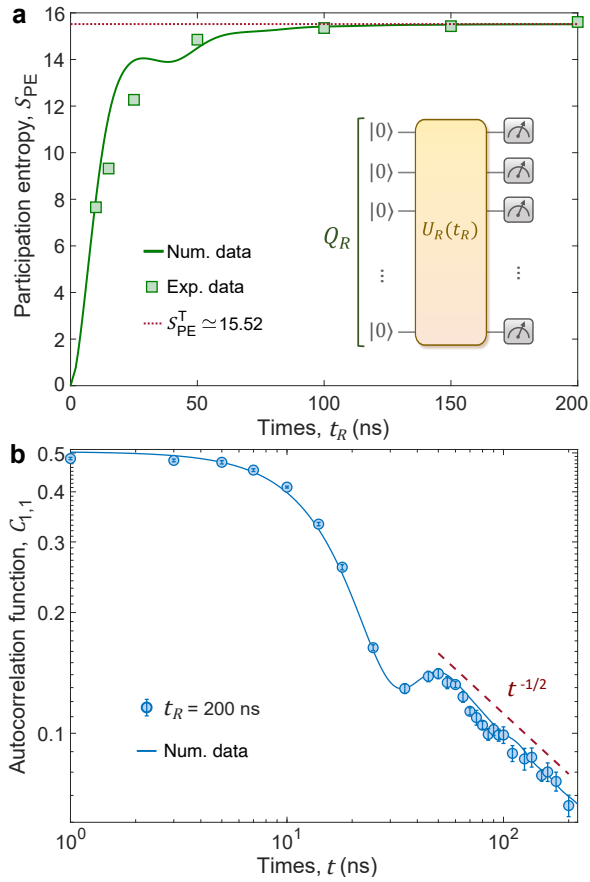


FIG. 2. **Observation of diffusive transport.** **a**, Experimental verification of preparing the states via the time evolution of participation entropy. Here, we chose $Q_R = \{Q_{1,\uparrow}, Q_{2,\uparrow}, \dots, Q_{12,\uparrow}, Q_{2,\downarrow}, Q_{3,\downarrow}, \dots, Q_{12,\downarrow}\}$ with total 23 qubits. The inset of **a** shows the corresponding quantum circuit. The dotted horizontal line represents the participation entropy for Haar-random states, i.e., $S_{PE}^T \simeq 15.519$. **b**, Experimental results of the autocorrelation function $C_{1,1}(t)$ for the qubit ladder with $L = 12$, which are measured by performing the quantum circuit shown in Fig. 1 **c** and **d**. Here, we consider the state generated from $\hat{U}_R(t_R)$ with $t_R = 200$ ns, which is approximate to a Haar-random state. Markers are experimental data. The solid line is the numerical simulation of the correlation function $C_{1,1}$ at infinite temperature. The dashed line represents a power-law decay $t^{-1/2}$. Error bars represent the standard deviation.

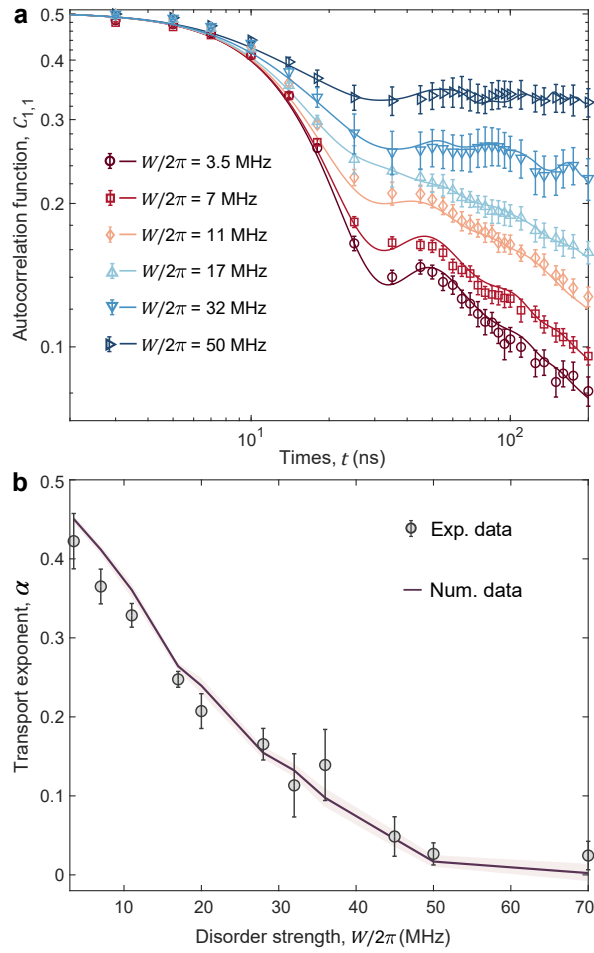


FIG. 3. Subdiffusive transport on the superconducting qubit ladder with disorder. **a**, The time evolution of autocorrelation function $C_{1,1}(t)$ for the qubit ladder with $L = 12$ and different values of disorder strength W , ranging from $W/2\pi = 35$ MHz ($W/\overline{J_{\parallel}} \simeq 0.5$) to $W/2\pi = 70$ MHz ($W/\overline{J_{\parallel}} \simeq 9.6$). Markers (lines) are experimental (numerical) data. **b**, Transport exponent α as a function of W obtained from fitting the data of $C_{1,1}(t)$. Error bars (experimental data) and shaded regions (numerical data) represent the standard deviation.

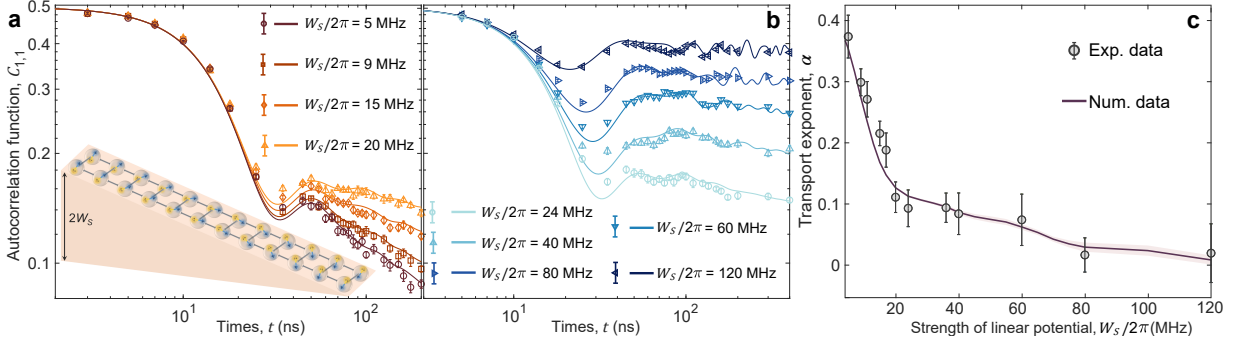


FIG. 4. **Subdiffusive transport on the superconducting qubit ladder with linear potential.** **a**, Time evolution of autocorrelation function $C_{1,1}(t)$ for the tilted qubit ladder with $L = 12$ and $W_S/2\pi \leq 20$ MHz. **b** is similar to **a** but for the data with $W_S/2\pi \geq 24$ MHz. Markers (lines) are experimental (numerical) data. **c**, Transport exponent α as a function of W_S . For $W_S/2\pi \leq 20$ MHz and $W_S/2\pi \geq 24$ MHz, the exponent α is extracted from fitting the data of $C_{1,1}(t)$ with the time window $t \in [50 \text{ ns}, 200 \text{ ns}]$ and $t \in [100 \text{ ns}, 400 \text{ ns}]$, respectively. Error bars (experimental data) and shaded regions (numerical data) represent the standard deviation.

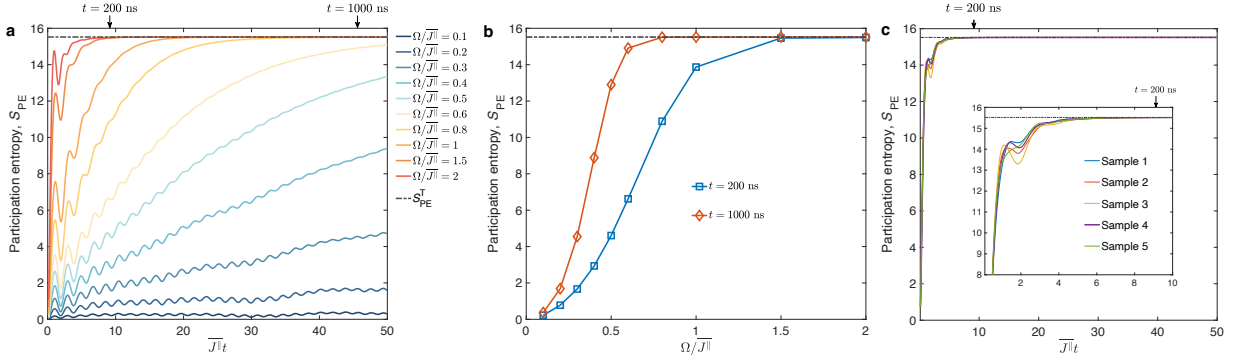


FIG. 5. **Impact of driving amplitude and phases of microwave pulse on the generation of Haar-random states.** **a**, The time evolution of the participation entropy S_{PE} for different driving amplitude Ω . **b**, The value of S_{PE} at two evolved times $t = 200$ ns and 1000 ns, as a function of Ω . **c**, The dynamics of S_{PE} with the phases of the microwave pulse drawn from $[-\pi, \pi]$. Here, we present the numerical data of 5 different samples of the phases. The inset show the dynamics in a shorter time interval. The horizontal dashed line represents the participation entropy for Haar-random states $S_{PE}^T \approx 15.519$.

Supplementary Information for Probing spin hydrodynamics on a superconducting quantum simulator

Yun-Hao Shi,^{1,2,3,*} Zheng-Hang Sun,^{1,2,*} Yong-Yi Wang,^{1,2,*} Zheng-An Wang,^{3,4} Yu-Ran Zhang,⁵ Wei-Guo Ma,^{1,2} Hao-Tian Liu,^{1,2} Kui Zhao,³ Jia-Cheng Song,^{1,2} Gui-Han Liang,^{1,2} Zheng-Yang Mei,^{1,2} Jia-Chi Zhang,^{1,2} Hao Li,³ Chi-Tong Chen,^{1,2} Xiaohui Song,¹ Jieci Wang,⁶ Guangming Xue,³ Haifeng Yu,³ Kaixuan Huang,^{3,†} Zhongcheng Xiang,^{1,2,4,‡} Kai Xu,^{1,2,3,4,7,8,§} Dongning Zheng,^{1,2,4,7,8} and Heng Fan^{1,2,3,4,7,8,¶}

¹*Institute of Physics, Chinese Academy of Sciences, Beijing 100190, China*

²*School of Physical Sciences, University of Chinese Academy of Sciences, Beijing 100049, China*

³*Beijing Academy of Quantum Information Sciences, Beijing 100193, China*

⁴*Hefei National Laboratory, Hefei 230088, China*

⁵*School of Physics and Optoelectronics, South China University of Technology, Guangzhou 510640, China*

⁶*Department of Physics and Key Laboratory of Low Dimensional Quantum Structures and Quantum Control of Ministry of Education, Hunan Normal University, Changsha, Hunan 410081, China*

⁷*Songshan Lake Materials Laboratory, Dongguan, Guangdong 523808, China*

⁸*CAS Center for Excellence in Topological Quantum Computation, UCAS, Beijing 100190, China*

CONTENTS

Supplementary Note 1. Model and Hamiltonian	2
Supplementary Note 2. Wiring information	4
Supplementary Note 3. XY drive in superconducting circuits	4
A. Single-qubit XY drive	4
B. Generation and manipulation	8
C. Origin of multi-qubit crosstalk	8
D. Measurement and correction of crosstalk	11
Supplementary Note 4. The effect of decoherence	12
Supplementary Note 5. XY drive approach to generate Haar-random states	13
Supplementary Note 6. Finite-size effect for the spin transport in the clean superconducting qubit ladder	15
Supplementary Note 7. Finite-time effect for the spin transport in disordered systems	16
Supplementary Note 8. Additional numerics and discussions	16

* These authors contributed equally to this work.

† huangkx@baqis.ac.cn

‡ zcxiang@iphy.ac.cn

§ kaixu@iphy.ac.cn

¶ hfan@iphy.ac.cn

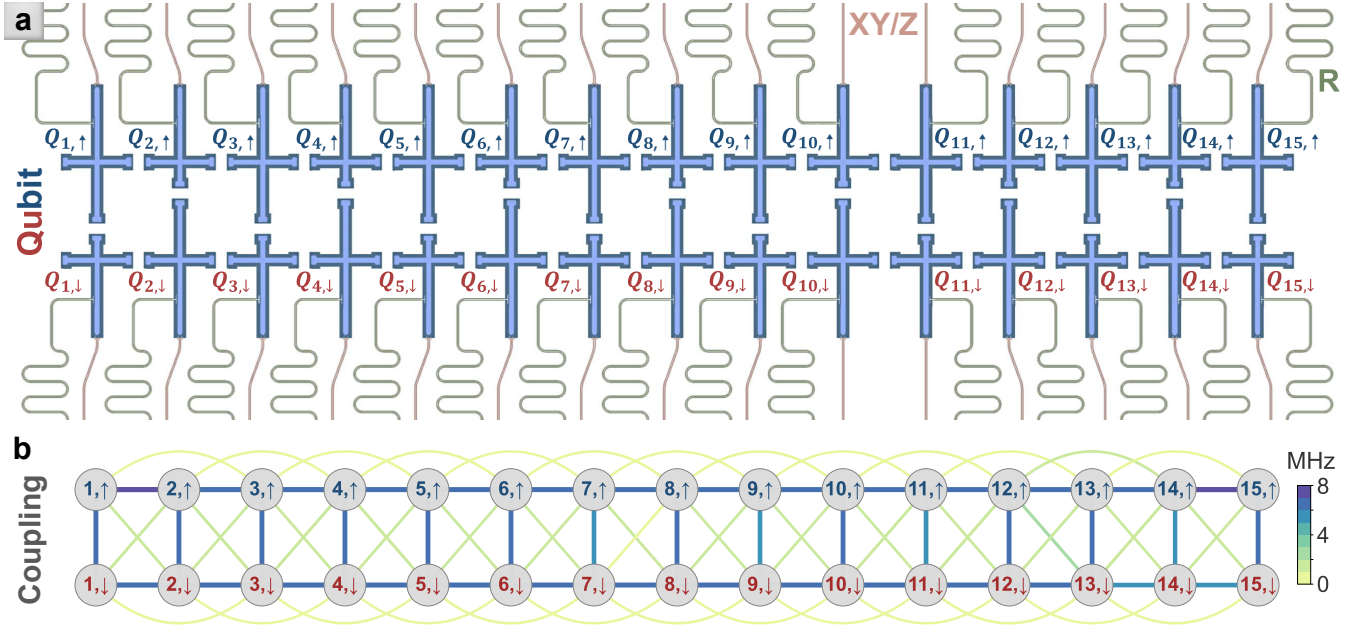


FIG. S1. **Schematic and coupling strengths of the chip.** **a**, The ladder-type chip with 30 superconducting qubits arranged in two coupled chains. Each qubit, coupled to an independent readout resonator R, has an independent microwave line for XY and Z controls. **b**, Coupling strengths including the NN and NNN hopping couplings, which are measured by swapping experiments at the resonant frequency $\omega_{\text{ref}} \approx 4.534\text{GHz}$.

Supplementary Note 1. MODEL AND HAMILTONIAN

In this experiment, we use a ladder-type superconducting quantum processor with 30 programmable superconducting transmon qubits, which is identical to the device in ref. [22]. The optical micrograph and coupling strengths of the chip are shown in Fig. S1, and the device parameters are listed in Table S1. The Hamiltonian of the total system can be essentially described by a Bose-Hubbard model of a ladder

$$\hat{H}_{\text{BH}} = \sum_{i=1}^N \hbar h_i \hat{a}_i^\dagger \hat{a}_i - \frac{E_{C,j}}{2} \hat{a}_j^\dagger \hat{a}_j^\dagger \hat{a}_j \hat{a}_j + \hat{H}_I, \quad (\text{S1})$$

where \hbar is the reduced Planck constant, N is the total number of qubits, \hat{a}^\dagger (\hat{a}) denotes the bosonic creation (annihilation) operator, h_j is the tunable on-site potential, $E_{C,j}$ denotes the on-site charge energy, representing the magnitude of anharmonicity, and \hat{H}_I is the Hamiltonian for the interactions between qubits. For qubits connected in a ladder-type with two coupled chains (' \uparrow ' and ' \downarrow '), the interaction Hamiltonian \hat{H}_I is mainly derived from the nearest-neighbor (NN) rung (vertical, ' \perp ') and intrachain (parallel, ' \parallel ') hopping couplings, namely

$$\hat{H}_\perp = \sum_{j=1}^L \hbar J_j^\perp (\hat{a}_{j,\uparrow}^\dagger \hat{a}_{j,\downarrow} + \text{H.c.}), \quad (\text{S2})$$

$$\hat{H}_\parallel = \sum_{m \in \{\uparrow, \downarrow\}} \sum_{j=1}^{L-1} \hbar J_{j,m}^\parallel (\hat{a}_{j,m}^\dagger \hat{a}_{j+1,m} + \text{H.c.}), \quad (\text{S3})$$

where $L = N/2$ is the length of each chain, J_j^\perp and $J_{j,m}^\parallel$ are the NN rung and intrachain coupling strengths. The mean values of $J_j^\perp/2\pi$ and $J_{j,m}^\parallel/2\pi$ are 6.6 MHz and 7.3 MHz, respectively. In addition, it is inevitable that small next-nearest-neighbor (NNN) interactions are present, including the hopping interactions between the diagonal qubits of the upper and lower chains (' \times ', diagonal down ' \searrow ' and diagonal up ' \swarrow ') and between NNN qubits on each chain (' \cap '), and the corresponding Hamiltonians

are expressed as

$$\hat{H}_\times = \sum_{j=1}^{L-1} \hbar J_j^\setminus (\hat{a}_{j,\uparrow}^\dagger \hat{a}_{j+1,\downarrow} + \text{H.c.}) + \hbar J_j^\prime (\hat{a}_{j,\downarrow}^\dagger \hat{a}_{j+1,\uparrow} + \text{H.c.}), \quad (\text{S4})$$

$$\hat{H}_\square = \sum_{m \in \{\uparrow, \downarrow\}} \sum_{j=1}^{L-2} \hbar J_{j,m}^\square (\hat{a}_{j,m}^\dagger \hat{a}_{j+2,m} + \text{H.c.}), \quad (\text{S5})$$

where J_j^\setminus , J_j^\prime and $J_{j,m}^\square$ are the strengths of diagonal down, diagonal up and parallel NNN hopping interactions, respectively. In short, for numerical simulations, we consider $\hat{H}_I = \hat{H}_\perp + \hat{H}_\parallel + \hat{H}_\times + \hat{H}_\square$.

In our quantum processor, the anharmonicity (≥ 200 MHz) is much greater than the coupling interaction and the model can be viewed as a ladder-type lattice of hard-core bosons [52], i.e., the Eq. (1) in the main text. However, in principle, the leakage to higher occupation states can be possibly induced by the finite value of the ratio between the averaged anharmonicity and coupling strength, i.e., $\overline{E_C}/\overline{J}$. To qualitatively characterize whether the Bose-Hubbard model (S1) can be approximate as the hard-core bosons, we consider the dynamics of the summation of the probability $\sum_{\max(\vec{s})=1} p(\vec{s})$ with \vec{s} denoting a configuration of product state. For instance, $\vec{s} = (1, 0, 1, 0, \dots, 1, 0)$ corresponds to the Néel state $|\vec{s}\rangle = |1010\dots10\rangle$. If the system exactly becomes a hard-core bosonic model, $\sum_{\max(\vec{s})=1} p(\vec{s}) = 1$. Here, we numerically simulate the dynamics of $\sum_{\max(\vec{s})=1} p(\vec{s})$ for the Hamiltonian of the superconducting circuit with experimentally measured hopping interactions and anharmonicity. As an example, we adopt the system size $L = 16$ and a half-filling product state as the initial state $|\psi_0\rangle$ (see the inset of Fig. S2a). The results are plotted in Fig. S2a. One can see that the summation of the probabilities for the states with higher occupations, i.e., $\sum_{\max(\vec{s})>1} p(\vec{s}) = 1 - \sum_{\max(\vec{s})=1} p(\vec{s})$, only reach a relatively small value ~ 0.03 , with the evolved time $t \simeq 200$ ns. Moreover, we numerically simulate the time evolution of the particle number $\langle n(t) \rangle \equiv \langle \psi(t) | \hat{n} | \psi(t) \rangle = \langle \psi(t) | \sum_i \hat{n}_i | \psi(t) \rangle$, with $\hat{n}_i \equiv |0\rangle_i \langle 0| + |1\rangle_i \langle 1|$, up to the experimental time scales $t \simeq 200$ ns. The results are displayed in Fig. S2b. We emphasize that only the occupations of the states $|0\rangle$ and $|1\rangle$ are considered in the definition of \hat{n}_i , while the finite $\overline{E_C}/\overline{J}$ allows the possibility of the leakage to the states with higher occupations, such as $|2\rangle$. Consequently, the decay of $\langle n(t) \rangle$ shown in Fig. S2 quantifies the leakage induced by the finite $\overline{E_C}/\overline{J}$. The stable value of $n(t)/2L$ with $t \simeq 200$ ns is about 0.4966, indicating a moderate impact of the leakage on the conservation of the particle number. In short, the results in Fig. S2 suggest that hard-core bosonic Hamiltonian (1) in the main text, with a conservation of the particle number, can efficiently describe our superconducting quantum simulator.

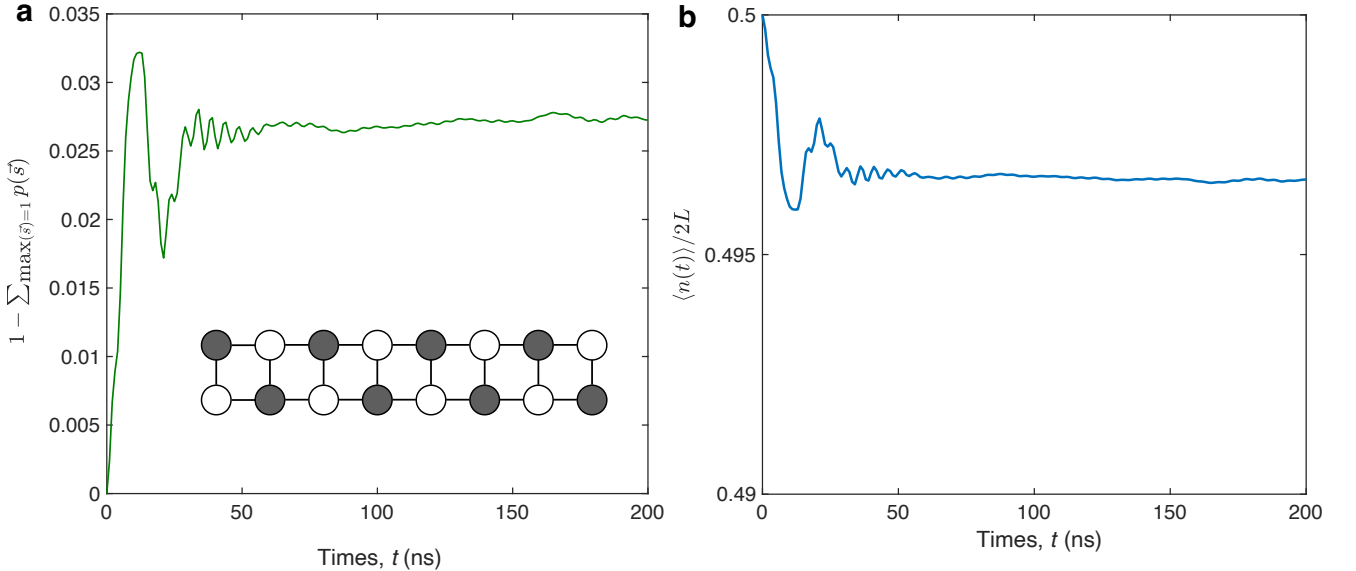


FIG. S2. **Demonstrate of hard-core bosonic model.** **a**, Time evolution of $\sum_{\max(\vec{s})=1} p(\vec{s})$ for the Hamiltonian of the superconducting circuit described by the Bose-Hubbard model (S1), with a system size $L = 8$. The inset shows a schematic of the chosen initial state, where the sites represented with solid black circles are initialized by the state $|1\rangle$, and the remainder sites are initialized by $|0\rangle$. **b**, The dynamics of the particle number $\langle n(t) \rangle$ for the Hamiltonian of the superconducting circuit with a system size $L = 8$.

Parameter	Median	Mean	Stdev.	Units
Qubit maximum frequency	5.025	5.032	0.240	GHz
Qubit idle frequency	4.723	4.728	0.346	GHz
Qubit anharmonicity $-E_C/(2\pi\hbar)$	-0.222	-0.222	0.022	GHz
Readout frequency	6.715	6.714	0.061	GHz
Mean energy relaxation time \bar{T}_1	33.2	32.1	7.5	μs
Pure dephasing time at idle frequency T_2^*	1.0	2.4	4.2	μs
Mean NN hopping coupling strength (vertical) \bar{J}^\perp	6.7	6.6	0.2	MHz
Mean NN hopping coupling strength (parallel) \bar{J}^\parallel	7.2	7.3	0.1	MHz
Mean NNN hopping coupling strength (diagonal) \bar{J}^\times	1.5	1.5	0.3	MHz
Mean NNN hopping coupling strength (parallel) \bar{J}^\cap	0.6	0.7	0.2	MHz
Readout fidelity of state $ 0\rangle$	95.2	91.4	9.6	%
Readout fidelity of state $ 1\rangle$	88.5	84.7	9.3	%

TABLE S1. List of device parameters.

Supplementary Note 2. WIRING INFORMATION

The typical wiring information is shown in Fig. S3, in which from up to down are the control lines of qubit (XY and Z), readout, and Josephson parametric amplifier (JPA), respectively. From left to right, the ambient temperature decreases from room temperature to 12mK in a BlueFors XLD-1000 dilution refrigerator. We combine the high-frequency XY signal with the low-frequency Z bias by using directional couplers at room temperature. The XY signals are generated via frequency mixing. In detail, we use the IQ mixer to mix the intrinsic local oscillation (LO) from a microwave signal source and the IQ signals generated from two channels of arbitrary waveform generator (AWG). The output microwave signal is programmable, which depends on the pulses written into IQ signals. The joint readout signals are sent through the transmission line and amplified by the JPA, a cryo low-noise amplifier (LNA) and a room-temperature RF amplifier (RFA), and finally demodulated by the analog-digital converter (ADC).

Supplementary Note 3. XY DRIVE IN SUPERCONDUCTING CIRCUITS

A. Single-qubit XY drive

A transmon qubit is composed of a capacitance C and a nonlinear inductance L (Josephson junction or SQUID). Its Lagrangian \mathcal{L}_0 and Hamiltonian H_0 can be written as

$$\mathcal{L}_0 = \frac{Q^2}{2C} - \frac{\Phi^2}{2L} \quad (\text{S6})$$

$$H_0 = \frac{Q^2}{2C} + \frac{\Phi^2}{2L}, \quad (\text{S7})$$

where $Q = \partial\mathcal{L}_0/\partial\dot{\Phi} = C\dot{\Phi}$ denotes the charge, and Φ is the magnetic flux of the circuit. Here, the nonlinear inductance of the Josephson junction with energy E_J can be written as $L = L_c/\cos(2\pi\Phi/\Phi_0)$, where $\Phi_0 = \hbar\pi/e$ is the superconducting flux quantum, $e \approx 1.602 \times 10^{-19}\text{C}$ is the electron charge, and $L_c = \Phi_0^2/(4\pi^2 E_J)$ is the constant inductance. This nonlinear inductance can be easily derived from the definition $L = d\Phi/dI$ and the Josephson equation $I = I_c \sin(2\pi\Phi/\Phi_0)$ with $I_c = 2\pi E_J/\Phi_0$ being the Josephson critical current.

Considering the weak flux Φ , one can use the approximation $\cos(2\pi\Phi/\Phi_0) \simeq 1 - (2\pi\Phi/\Phi_0)^2/2$ and reduce the Hamiltonian Eq. (S7) into $H_0 \simeq \frac{Q^2}{2C} + \frac{\Phi^2}{2L_c} - \frac{\pi^2\Phi^4}{4L_c\Phi_0^2}$, which can be viewed as a harmonic oscillator with $o(\Phi^4)$ perturbation. Using canonical quantization, one can introduce

$$\begin{cases} \hat{Q} = iQ_{\text{zpf}}(\hat{a}^\dagger - \hat{a}) \\ \hat{\Phi} = \Phi_{\text{zpf}}(\hat{a}^\dagger + \hat{a}) \end{cases} \quad (\text{S8})$$

with $Q_{\text{zpf}} = \sqrt{\hbar(C/L_c)^{1/2}/2}$ and $\Phi_{\text{zpf}} = \sqrt{\hbar(L_c/C)^{1/2}/2}$ being the zero point fluctuation of the charge and flux operators,

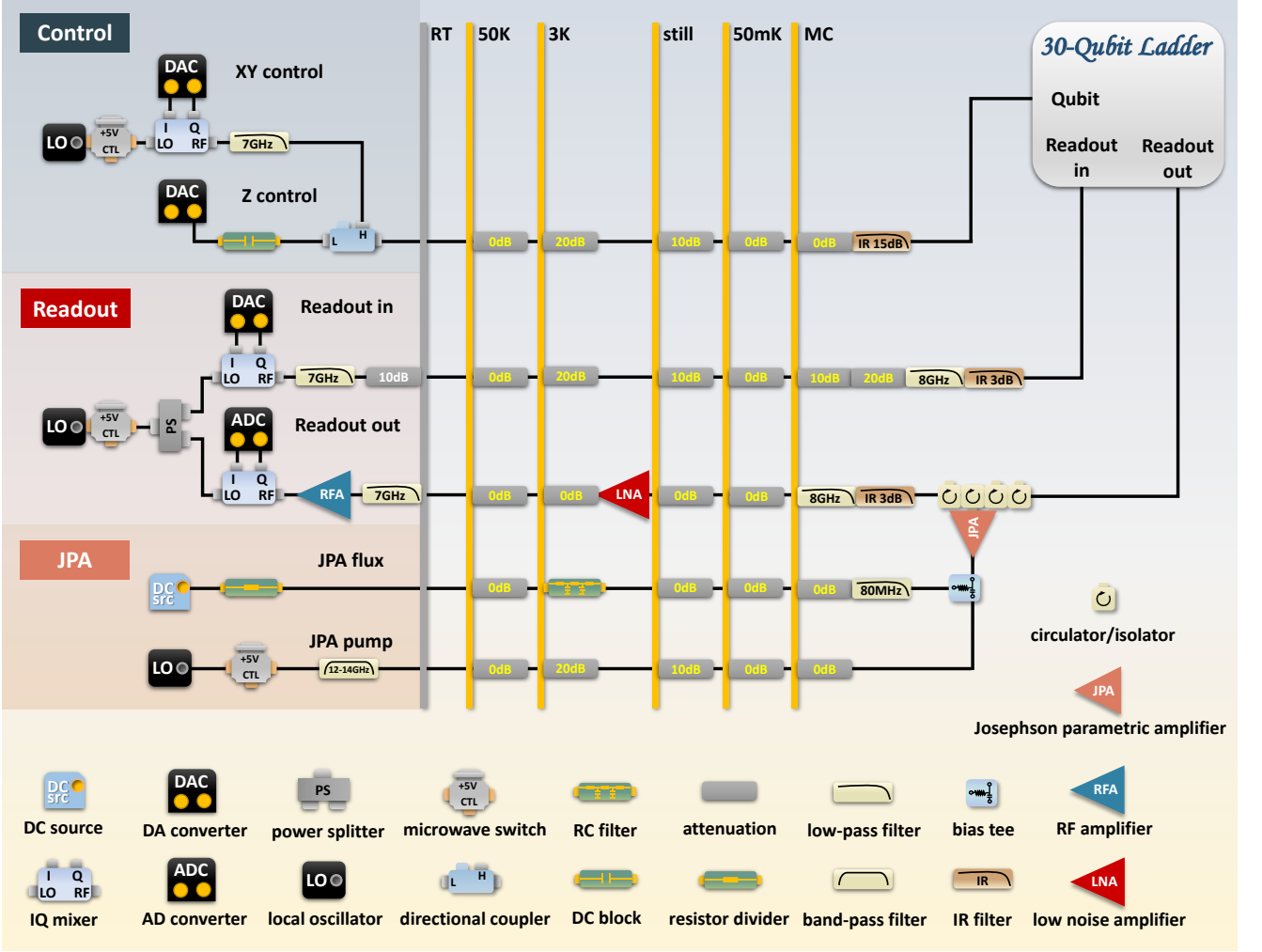


FIG. S3. Schematic diagram of the experimental system and wiring information.

respectively. The quantized Hamiltonian thus is (the constant term is omitted):

$$\hat{H}_0 = \hbar\omega\hat{a}^\dagger\hat{a} - \frac{E_C}{2}\hat{a}^\dagger\hat{a}^\dagger\hat{a}\hat{a}, \quad (\text{S9})$$

where $\omega = (\sqrt{8E_C E_J} - E_C)/\hbar$ denotes the qubit frequency, and $E_C = e^2/(2C)$ is the charging energy that represents the magnitude of anharmonicity. For a single Josephson junction, E_J is not tunable, while for a SQUID with two junctions, it depends on the external flux Φ_{ext} applied to the junction region. In the experiments, we can adjust the qubit frequency ω via the external fast flux bias applied to the Z control line.

When a time-dependent driving voltage $V_d(t)$ is added into a transmon qubit (Fig. S4), the driving current I_d can be split into the qubit capacitance term I_C and the Josephson junction term I_J . Meanwhile, according to Kirchhoff voltage law, the total voltage reduction through either of the two branches must be zero. Thus, one can obtain the following motion equation

$$\begin{cases} I_d = I_C + I_J \\ -\dot{V}_d + \frac{I_d}{C_d} + \frac{I_C}{C} = 0 \\ -\dot{V}_d + \frac{I_d}{C_d} + LI\ddot{\Phi} = 0 \end{cases} \Rightarrow \ddot{\Phi} + \frac{1}{C_\Sigma L}\Phi - \frac{C_d\dot{V}_d(t)}{C_\Sigma} = 0, \quad (\text{S10})$$

where $C_\Sigma = C + C_d$, $\Phi = LI_J$. Here C , C_d and L are the qubit capacitance, the driving capacitance, and the nonlinear inductance, respectively. The above equation can be viewed as the Euler-Lagrange equation: $\frac{\partial \mathcal{L}_{\text{driven}}}{\partial \Phi} - \frac{d}{dt} \frac{\partial \mathcal{L}_{\text{driven}}}{\partial \dot{\Phi}} = 0$, where the Lagrangian of this driven qubit can be constructed as

$$\mathcal{L}_{\text{driven}} = \frac{1}{2}C\dot{\Phi}^2 + \frac{1}{2}C_d(V_d(t) - \dot{\Phi})^2 - \frac{\Phi^2}{2L}, \quad (\text{S11})$$

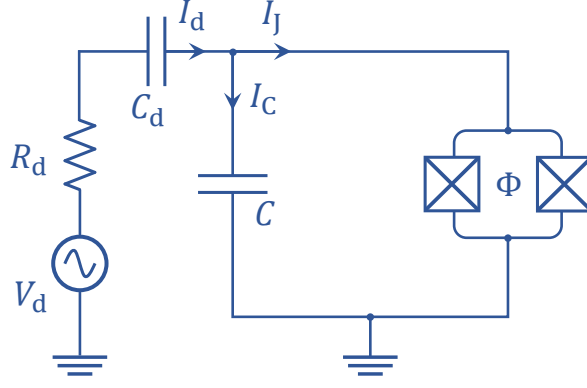


FIG. S4. **Circuit diagram of a driven transmon qubit.** The qubit is coupled to a time-dependent driving voltage V_d . The capacitances of the qubit and the drive are labeled as C and C_d , respectively. The magnetic flux threading the loop is denoted as Φ . The driving current I_d is split into I_C and I_J .

where C_d is the driving capacitance. In Eq. (S11), the first term represents the charge energy of C , the second term denotes the charge energy of C_d caused by induced electromotive force, and the last term is the inductance energy of L .

To obtain the Hamiltonian, we first calculate the conjugate to the position (flux) Φ , namely the canonical momentum (charge) $\tilde{Q} = \partial \mathcal{L}_{\text{driven}} / \partial \dot{\Phi} = C_{\Sigma} \dot{\Phi} - C_d V_d(t)$, and thus

$$H_{\text{driven}} = \tilde{Q} \dot{\Phi} - \mathcal{L}_{\text{driven}} = \frac{\tilde{Q}^2}{2C_{\Sigma}} + \frac{\Phi^2}{2L} + \frac{\tilde{Q} C_d V_d(t)}{C_{\Sigma}}. \quad (\text{S12})$$

Using the canonical quantization procedure like Eq. (S8), we introduce $\hat{Q} = i\tilde{Q}_{\text{zpf}}(\hat{a}^{\dagger} - \hat{a})$ and $\hat{\Phi} = \Phi_{\text{zpf}}(\hat{a}^{\dagger} + \hat{a})$ to quantize the driven system, where $\tilde{Q}_{\text{zpf}} = \sqrt{\hbar(C_{\Sigma}/L_c)^{1/2}}/2$ and $\Phi_{\text{zpf}} = \sqrt{\hbar(L_c/C_{\Sigma})^{1/2}}/2$. Hence, the Hamiltonian becomes

$$\hat{H}_{\text{driven}} = \hbar\omega\hat{a}^{\dagger}\hat{a} - \frac{E_C}{2}\hat{a}^{\dagger}\hat{a}^{\dagger}\hat{a}\hat{a} + i\hbar\Omega(t)(\hat{a}^{\dagger} - \hat{a}), \quad (\text{S13})$$

where $E_C = e^2/(2C_{\Sigma})$, $E_J = \Phi_0^2/(4\pi^2 L_c)$, $\omega = (\sqrt{8E_C E_J} - E_C)/\hbar$, $\Omega(t) = \epsilon V_d(t)$, $\epsilon = \tilde{Q}_{\text{zpf}} C_d / (\hbar C_{\Sigma})$. Here, we set the time-dependent driving $V_d(t) = -V_d \sin(\omega_d t + \phi) = \text{Im}\{V_d e^{-i(\omega_d t + \phi)}\}$, thus $\Omega(t) = i\Omega(e^{i(\omega_d t + \phi)} - e^{-i(\omega_d t + \phi)})/2$, where $\Omega = \epsilon V_d$ is so-called Rabi frequency. The parameter ϵ represents the Rabi frequency corresponding to the unit amplitude of the drive.

To solve the time evolution governed by the above time-dependent Hamiltonian, we consider the rotating frame which is generated by $\hat{U}_d(t) = e^{i\omega_d t \hat{a}^{\dagger} \hat{a}}$

$$\begin{aligned} \hat{H}_d &= \hat{U}_d(t) \hat{H}_{\text{driven}}(t) \hat{U}_d^{\dagger}(t) + i\hbar \left(\frac{d}{dt} \hat{U}_d(t) \right) \hat{U}_d^{\dagger}(t) \\ &\simeq \hbar\Delta \hat{a}^{\dagger} \hat{a} - \frac{E_C}{2} \hat{a}^{\dagger} \hat{a}^{\dagger} \hat{a} \hat{a} + \frac{\hbar\Omega}{2} (\hat{a}^{\dagger} e^{-i\phi} + \hat{a} e^{i\phi}), \end{aligned} \quad (\text{S14})$$

where $\Delta = \omega - \omega_d$ is the frequency detuning, and the rotating-wave approximation is adopted by ignoring high frequency oscillation $\pm 2\omega_d$.

With $\Delta = 0$ and $E_C \gg \Omega$, the large anharmonicity results in the resonant drive acting almost exclusively between the first two energy levels $|0\rangle$ and $|1\rangle$ without leakage to higher levels. Hence, considering the two-level qubit, we have

$$\hat{H}_d = \frac{\hbar\Omega}{2} (\hat{\sigma}^+ e^{-i\phi} + \hat{\sigma}^- e^{i\phi}), \quad (\text{S15})$$

where $\hat{\sigma}_j^+$ ($\hat{\sigma}_j^-$) is the raising (lowering) operator. If the qubit begins in the ground state $|0\rangle$, its time-dependent state during the unitary evolution is

$$|\psi_d(t)\rangle = e^{-\frac{i}{\hbar} \hat{H}_d t} |0\rangle = \cos \frac{\Omega t}{2} |0\rangle - i e^{i\phi} \sin \frac{\Omega t}{2} |1\rangle, \quad (\text{S16})$$

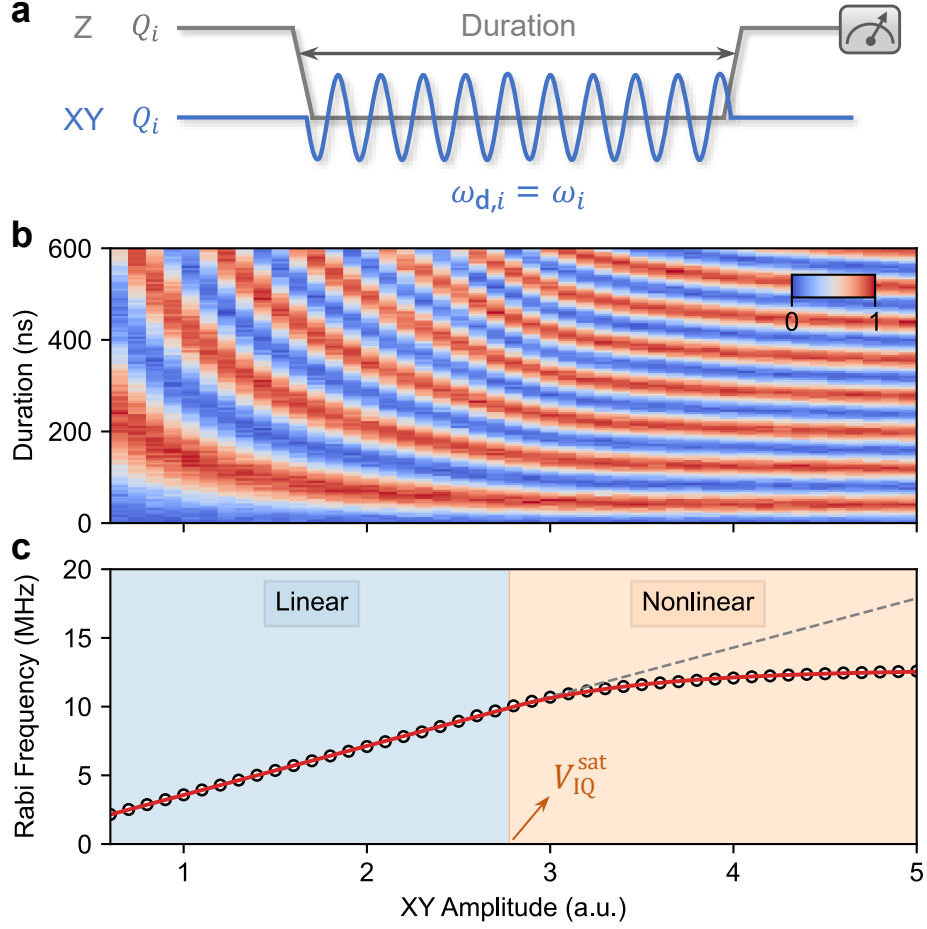


FIG. S5. **Typical experimental data of measuring the relationship between Rabi frequency and XY drive amplitude.** **a**, Experimental pulse sequence. Qubit is detuned from its idle frequency to the operating ω_i . Meanwhile, we apply resonant microwave drives on this qubit with scanning XY amplitude V_{IQ} and measure the vacuum Rabi oscillations shown in **b**. **b**, The heatmap of the probabilities of qubit in the state $|1\rangle$ as a function of duration and XY amplitude. **c**, For each XY drive amplitude, we fit the curve of vacuum Rabi oscillation by using Eq. (S17) to obtain the experimental Rabi frequency, denoted as black hollow circle. The red solid line is the result of fitting the experimental Rabi frequencies by using a smooth piecewise function and the grey dashed line implies the linear relationship between Rabi frequency and XY drive amplitude when the drive amplitude is less than V_{IQ}^{sat} .

and the probability of qubit in $|1\rangle$ is given by $P_1(t) = \sin^2(\Omega t/2) = [1 - \cos(\Omega t)]/2$. Considering the energy relaxation, the envelope of $P_1(t)$ will decay in a dissipative evolution and thus

$$P_1(t) = \frac{1}{2} \left[1 - e^{-\frac{t}{T_1}} \cos(\Omega t) \right], \quad (\text{S17})$$

where T_1 is the energy relaxation time that depends on the qubit frequency ω . In order to obtain the Rabi frequency Ω , one can fit the data of $P_1(t)$ by using the form of function $A \exp(-t/T_1) \cos(\Omega t) + B$. Typical experimental data of calibrating XY drive with different driving amplitudes are displayed in Fig. S5.

The above results are based on the resonance condition $\omega = \omega_d$. If the detuning $\Delta = \omega - \omega_d \neq 0$, the effective Rabi frequency will be

$$\Omega_R = \sqrt{\Delta^2 + \Omega^2}. \quad (\text{S18})$$

Therefore, to obtain the correct Rabi frequency when $\omega = \omega_d$, we should find the corresponding Z pulse amplitude that makes the qubit resonate with the microwave before calibrating XY drive. This step can be easily achieved via spectroscopy experiment or Rabi oscillation by scanning the Z pulse amplitude of the qubit.

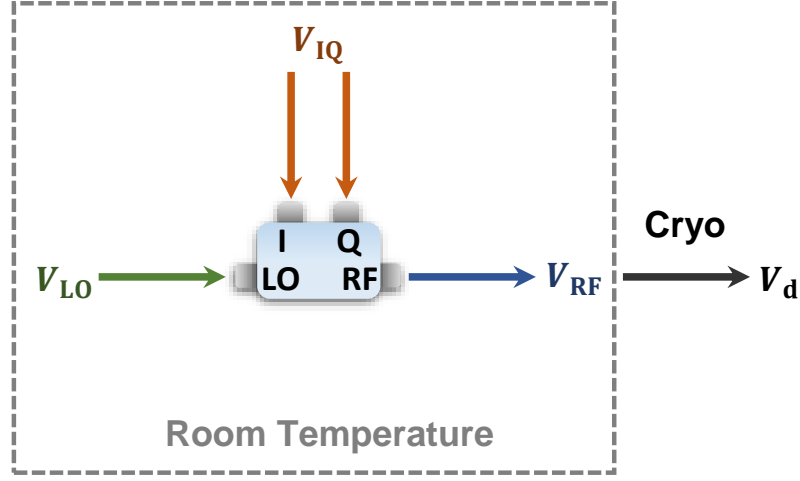


FIG. S6. **Generation of XY drive via frequency mixing.** The intrinsic local oscillation (LO) is generated from a microwave signal source, while the input IQ signals are generated from two channels of the arbitrary waveform generator. The whole circuit is mixed at room temperature and then goes into cryoelectronics (dilution refrigerator). If the amplitude of LO is fixed, the output pulse amplitude will be proportional to the amplitude of IQ signals in small amplitude cases where the IQ mixer is in a linear work region.

B. Generation and manipulation

As shown in Fig. S6, we generate XY drive pulse by using IQ mixer. The output driving pulse results from mixing the IQ signals with a intrinsic LO (Fig. S6). Although the Rabi frequency Ω is proportional to the actual driving amplitude V_d , the relationship between Ω and the input amplitude of IQ signals V_{IQ} is not always linear due to the semiconductor nature of the IQ mixer (GaAs and similar semiconductor materials). When V_{IQ} is relatively small, IQ mixer is in the linear work region and $V_d \propto V_{IQ}$ satisfies. However, the strong amplitude leads to a nonlinear relationship between V_d and V_{IQ} , so that $\Omega \propto V_{IQ}$ is not valid in the saturation region. This may be caused by the velocity saturation of carriers in the IQ mixer. In order to analytically describe Ω versus V_{IQ} , we impose the following smooth piecewise function and its inverse:

$$\Omega = \begin{cases} \eta V_{IQ}, & (V_{IQ} \leq V_{IQ}^{\text{sat}}) \\ \Omega_{\text{max}} - (\Omega_{\text{max}} - \eta V_{IQ}^{\text{sat}}) e^{-\frac{\eta(V_{IQ} - V_{IQ}^{\text{sat}})}{\Omega_{\text{max}} - \eta V_{IQ}^{\text{sat}}}}, & (V_{IQ} > V_{IQ}^{\text{sat}}) \end{cases} \quad (\text{S19})$$

$$V_{IQ} = \begin{cases} \frac{1}{\eta} \Omega, & (\Omega \leq \eta V_{IQ}^{\text{sat}}) \\ V_{IQ}^{\text{sat}} + \left(\frac{\Omega_{\text{max}}}{\eta} - V_{IQ}^{\text{sat}}\right) \ln\left(\frac{\Omega_{\text{max}} - \eta V_{IQ}^{\text{sat}}}{\Omega_{\text{max}} - \Omega}\right), & (\Omega > \eta V_{IQ}^{\text{sat}}) \end{cases} \quad (\text{S20})$$

where η , V_{IQ}^{sat} and Ω_{max} are the parameters to be fitted. Here η is the slope in linear region that represents the Rabi frequency corresponding to the unit amplitude of XY driving (IQ signals), V_{IQ}^{sat} denotes the critical amplitude before entering the saturation region of IQ mixer, and Ω_{max} is the maximum Rabi frequency when $V_{IQ} \rightarrow \infty$.

C. Origin of multi-qubit crosstalk

Now we consider two driven qubits Q_i and Q_j in the circuit (see Fig. S7). The total Lagrangian can be expressed as

$$\mathcal{L}_{\text{driven}}^{(i,j)} = \sum_{q=i,j} \left(\frac{1}{2} C_q \dot{\Phi}_q^2 - \frac{\Phi_q^2}{2L_q} \right) + \frac{1}{2} C_{d,i} (V_{d,i}(t) - \dot{\Phi}_i)^2 + \frac{1}{2} C_{d,j} (V_{d,j}(t) - \dot{\Phi}_j)^2 + \frac{1}{2} C_{ij} (\dot{\Phi}_j - \dot{\Phi}_i)^2, \quad (\text{S21})$$

where C_{ij} is the coupling capacitance. The corresponding canonical momentums are

$$\begin{bmatrix} \tilde{Q}_i \\ \tilde{Q}_j \end{bmatrix} = \begin{bmatrix} \frac{\partial \mathcal{L}_{\text{driven}}^{(i,j)}}{\partial \dot{\Phi}_i} \\ \frac{\partial \mathcal{L}_{\text{driven}}^{(i,j)}}{\partial \dot{\Phi}_j} \end{bmatrix} = \begin{bmatrix} C_{\Sigma_i} + C_{ij} & -C_{ij} \\ -C_{ij} & C_{\Sigma_j} + C_{ij} \end{bmatrix} \begin{bmatrix} \dot{\Phi}_i \\ \dot{\Phi}_j \end{bmatrix} - \begin{bmatrix} C_{d,i} V_{d,i} \\ C_{d,j} V_{d,j} \end{bmatrix}, \quad (\text{S22})$$

where $C_{\Sigma_i} = C_i + C_{d,i}$ and $C_{\Sigma_j} = C_j + C_{d,j}$, and thus

$$\begin{bmatrix} \dot{\Phi}_i \\ \dot{\Phi}_j \end{bmatrix} = \frac{1}{\|\mathbf{C}\|} \begin{bmatrix} C_{\Sigma_j} + C_{ij} & C_{ij} \\ C_{ij} & C_{\Sigma_i} + C_{ij} \end{bmatrix} \begin{bmatrix} \tilde{Q}_i + C_{d,i}V_{d,i} \\ \tilde{Q}_j + C_{d,i}V_{d,i} \end{bmatrix}, \quad (\text{S23})$$

where $\|\mathbf{C}\| = C_{\Sigma_i}C_{\Sigma_j} + C_{\Sigma_i}C_{ij} + C_{\Sigma_j}C_{ij}$ is the determinant of the capacitance matrix $\mathbf{C} = \begin{bmatrix} C_{\Sigma_i} + C_{ij} & -C_{ij} \\ -C_{ij} & C_{\Sigma_j} + C_{ij} \end{bmatrix}$. Substituting Eq. (S23) into Eq. (S21), we obtain

$$\mathcal{L}_{\text{driven}}^{(i,j)} = \frac{\tilde{Q}_i^2}{2\tilde{C}_{\Sigma_i}} + \frac{\tilde{Q}_j^2}{2\tilde{C}_{\Sigma_j}} + \frac{\tilde{Q}_i\tilde{Q}_j}{\tilde{C}_{ij}}, \quad (\text{S24})$$

with the effective capacitance parameters

$$\tilde{C}_{\Sigma_i} = C_{\Sigma_i} + (C_{\Sigma_j}\|C_{ij}) = C_{\Sigma_i} + \frac{C_{\Sigma_j}C_{ij}}{C_{\Sigma_j} + C_{ij}}, \quad (\text{S25})$$

$$\tilde{C}_{\Sigma_j} = C_{\Sigma_j} + (C_{\Sigma_i}\|C_{ij}) = C_{\Sigma_j} + \frac{C_{\Sigma_i}C_{ij}}{C_{\Sigma_i} + C_{ij}}, \quad (\text{S26})$$

$$\tilde{C}_{ij} = \frac{C_{\Sigma_i}C_{ij} + C_{\Sigma_j}C_{ij} + C_{\Sigma_i}C_{\Sigma_j}}{C_{ij}}. \quad (\text{S27})$$

Then the total Hamiltonian is given by the Legendre transformation:

$$\begin{aligned} H_{\text{driven}}^{(i,j)} &= \tilde{Q}_i\dot{\Phi}_i + \tilde{Q}_j\dot{\Phi}_j - \mathcal{L}_{\text{driven}}^{(i,j)} \\ &= \sum_{q=i,j} \left(\frac{\tilde{Q}_q^2}{2\tilde{C}_{\Sigma_q}} + \frac{\Phi_q^2}{2L_q} \right) + \frac{\tilde{Q}_i\tilde{Q}_j}{\tilde{C}_{ij}} + \left(\frac{C_{d,i}}{\tilde{C}_{\Sigma_i}}V_{d,i}(t) + \frac{C_{d,j}}{\tilde{C}_{ij}}V_{d,j}(t) \right) \tilde{Q}_i + \left(\frac{C_{d,j}}{\tilde{C}_{\Sigma_j}}V_{d,j}(t) + \frac{C_{d,i}}{\tilde{C}_{ij}}V_{d,i}(t) \right) \tilde{Q}_j. \end{aligned} \quad (\text{S28})$$

Using canonical quantization, we introduce

$$\begin{cases} \hat{\tilde{Q}}_q = i\tilde{Q}_{\text{zpf},q}(\hat{a}_q^\dagger - \hat{a}_q) \\ \hat{\Phi}_q = \Phi_{\text{zpf},q}(\hat{a}_q^\dagger + \hat{a}_q) \end{cases} \quad (\text{S29})$$

with $q \in \{i, j\}$, $\tilde{Q}_{\text{zpf},q} = \sqrt{\hbar(\tilde{C}_{\Sigma_q}/L_{c,q})^{1/2}}/2$ and $\Phi_{\text{zpf},q} = \sqrt{\hbar(L_{c,q}/\tilde{C}_{\Sigma_q})^{1/2}}/2$. The quantized Hamiltonian thus is

$$\hat{H}_{\text{driven}}^{(i,j)} = \hat{H}_{\text{driven}}^{(i)} + \hat{H}_{\text{driven}}^{(j)} + \hat{H}_{\text{int}}^{(i,j)}, \quad (\text{S30})$$

$$\hat{H}_{\text{driven}}^{(q)} = \hbar\omega_q\hat{a}_q^\dagger\hat{a}_q - \frac{E_{C_q}}{2}\hat{a}_q^\dagger\hat{a}_q^\dagger\hat{a}_q\hat{a}_q + i\hbar\tilde{\Omega}_q(t)(\hat{a}_q^\dagger - \hat{a}_q), \quad q \in \{i, j\}, \quad (\text{S31})$$

$$\hat{H}_{\text{int}}^{(i,j)} = \hbar J_{i,j}(\hat{a}_i^\dagger - \hat{a}_i)(\hat{a}_j - \hat{a}_j^\dagger), \quad (\text{S32})$$

where the parameters are

$$\hbar\omega_q = \sqrt{8E_{C_q}E_{J_q}} - E_{C_q}, \quad E_{C_q} = \frac{e^2}{2\tilde{C}_q}, \quad E_{J_q} = \frac{\Phi_0^2}{4\pi^2L_{c,q}}, \quad (\text{S33})$$

$$J_{i,j} = \frac{\tilde{Q}_{\text{zpf},i}\tilde{Q}_{\text{zpf},j}}{\hbar\tilde{C}_{ij}} = \frac{\sqrt{\tilde{C}_{\Sigma_i}\tilde{C}_{\Sigma_j}}}{2\tilde{C}_{ij}} \sqrt{\left(\omega_i + \frac{E_{C_i}}{\hbar}\right)\left(\omega_j + \frac{E_{C_j}}{\hbar}\right)} \approx \frac{C_{ij}\sqrt{\omega_i\omega_j}}{2\sqrt{(C_{\Sigma_i} + C_{ij})(C_{\Sigma_j} + C_{ij})}}, \quad (\text{S34})$$

$$\tilde{\Omega}_i(t) = \epsilon_{ii} \left(V_{d,i}(t) + \frac{\epsilon_{ij}}{\epsilon_{ii}}V_{d,j}(t) \right), \quad \tilde{\Omega}_j(t) = \epsilon_{jj} \left(V_{d,j}(t) + \frac{\epsilon_{ji}}{\epsilon_{jj}}V_{d,i}(t) \right), \quad (\text{S35})$$

$$\epsilon_{ii} = \frac{\tilde{Q}_{\text{zpf},i}C_{d,i}}{\hbar\tilde{C}_{\Sigma_i}}, \quad \epsilon_{ij} = \frac{\tilde{Q}_{\text{zpf},i}C_{d,j}}{\hbar\tilde{C}_{ij}}, \quad \epsilon_{jj} = \frac{\tilde{Q}_{\text{zpf},j}C_{d,j}}{\hbar\tilde{C}_{\Sigma_j}}, \quad \epsilon_{ji} = \frac{\tilde{Q}_{\text{zpf},j}C_{d,i}}{\hbar\tilde{C}_{ij}}. \quad (\text{S36})$$

Focusing on Eqs. (S31), (S35) and (S36), one can notice that the local driving Hamiltonian of each qubit depends on both external drive $V_{d,i}(t)$ and $V_{d,j}(t)$ due to the presence of coupling capacitance. However, this crosstalk is usually very small. As an example, we take the typical values $C_{d,i} = C_{d,j} = 30$ aF, $C_i = C_j = 85$ fF and $C_{ij} = 0.25$ fF. Then we have

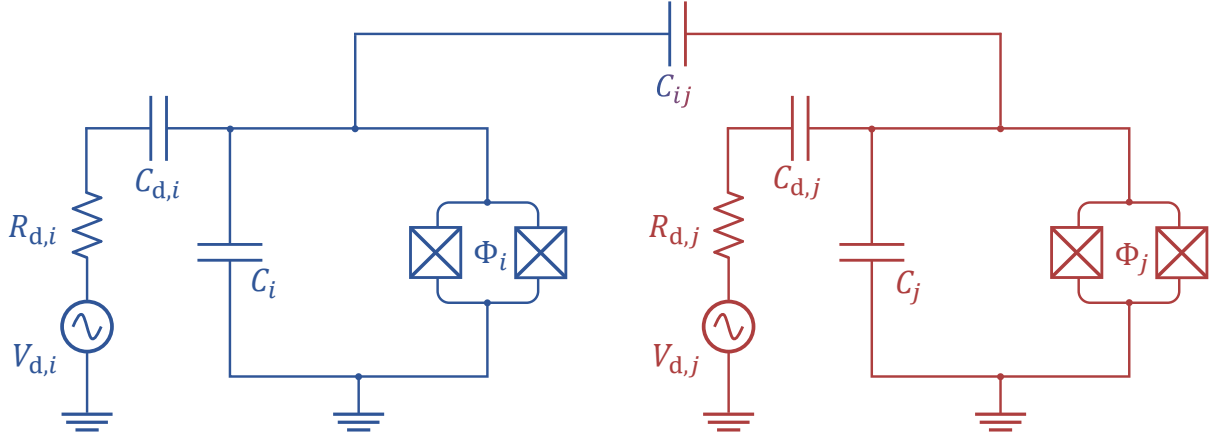


FIG. S7. **Circuit diagram of two driven transmon qubits.** Two qubits are labeled as Q_i and Q_j , which are coupled to their respective time-dependent driving voltages $V_{d,i}(t)$ and $V_{d,j}(t)$. The coupling capacitance between the two qubits is represented as C_{ij} , and Φ , C and C_d are the dominant mode flux, the capacitance of the qubit and the capacitance of the drive, respectively.

$\epsilon_{ij}/\epsilon_{ii} = \epsilon_{ji}/\epsilon_{jj} \approx 0.3\%$, suggesting a low level of this crosstalk. Given the above equations, we note that the local driving Hamiltonian of each qubit is subject to both external drive $V_{d,i}(t)$ and $V_{d,j}(t)$ due to the presence of coupling capacitance. However, this crosstalk is usually very small. In fact, most of the crosstalk comes from the classical microwave crosstalk. The total crosstalk is the sum of the classical microwave crosstalk and the crosstalk due to the coupling capacitance. In the following, we will establish a model to describe the total crosstalk and introduce an efficient method for measuring the crosstalk matrix.

When the microwave signal travels through the medium on the chip, it can be described by the following plane wave form (the medium is assumed to be homogeneous):

$$V_d(\mathbf{r}, t) = V_d(t)e^{i\mathbf{k}\cdot\mathbf{r}}. \quad (\text{S37})$$

Here the wave vector \mathbf{k} is generally complex, namely $\mathbf{k} = \mathbf{b} + i\mathbf{a}$, thus we have

$$i\mathbf{k}\cdot\mathbf{r} = -\mathbf{a}\cdot\mathbf{r} + i\mathbf{b}\cdot\mathbf{r}, \quad (\text{S38})$$

where the first term is the amplitude attenuation induced by the imaginary part of \mathbf{k} and the second term is the phase retardation caused by the real part. Here we define $\xi = \mathbf{a}\cdot\mathbf{r}$ is the amplitude attenuation factor and $\varphi = \mathbf{b}\cdot\mathbf{r}$ is the phase retardation.

As shown in Fig. S8, the signal $V_{d,i}(t)$ propagates from Q_i to Q_j with a factor $e^{-\xi_{ji}+i\varphi_{ji}}$ attached, which implies the classical microwave crosstalk of Q_i to Q_j . Similarly, the classical microwave crosstalk of Q_j to Q_i can be express as $V_{d,j}(t)e^{-\xi_{ij}+i\varphi_{ij}}$. Here we also consider the crosstalk caused by the coupling capacitance as Eq. (S35). Therefore, the total signals perceived by Q_i and Q_j are

$$\tilde{V}_{d,i}(t) = V_{d,i}(t) + \frac{\epsilon_{ij}}{\epsilon_{ii}}V_{d,j}(t) + V_{d,j}(t)e^{-\xi_{ij}+i\varphi_{ij}}, \quad (\text{S39})$$

$$\tilde{V}_{d,j}(t) = V_{d,j}(t) + \frac{\epsilon_{ji}}{\epsilon_{jj}}V_{d,i}(t) + V_{d,i}(t)e^{-\xi_{ji}+i\varphi_{ji}}, \quad (\text{S40})$$

or written in matrix form

$$\begin{bmatrix} \tilde{V}_{d,i}(t) \\ \tilde{V}_{d,j}(t) \end{bmatrix} = \begin{bmatrix} 1 & v_{ij}e^{i\varphi_{ij}} \\ v_{ji}e^{i\varphi_{ji}} & 1 \end{bmatrix} \begin{bmatrix} V_{d,i}(t) \\ V_{d,j}(t) \end{bmatrix} \quad (\text{S41})$$

with the definitions of $v_{ij}e^{i\varphi_{ij}} = \epsilon_{ij}/\epsilon_{ii} + e^{-\xi_{ij}+i\varphi_{ij}}$ and $v_{ji}e^{i\varphi_{ji}} = \epsilon_{ji}/\epsilon_{jj} + e^{-\xi_{ji}+i\varphi_{ji}}$. To generalize the above formula to the case of each qubit with crosstalks from all other qubits, we define the vectors $\tilde{\mathbf{V}}_d(t) = [\tilde{V}_{d,1}(t), \tilde{V}_{d,2}(t), \dots, \tilde{V}_{d,N}(t)]^T$ and $\mathbf{V}_d(t) = [V_{d,1}(t), V_{d,2}(t), \dots, V_{d,N}(t)]^T$, then

$$\tilde{\mathbf{V}}_d(t) = \mathbf{M}_V \mathbf{V}_d(t), \quad (\text{S42})$$

in which $\mathbf{M}_{\mathbf{V}}$ is the signal crosstalk matrix

$$\mathbf{M}_{\mathbf{V}} = \begin{bmatrix} 1 & v_{12}e^{i\varphi_{12}} & \dots & v_{1N}e^{i\varphi_{1N}} \\ v_{21}e^{i\varphi_{21}} & 1 & \dots & v_{2N}e^{i\varphi_{2N}} \\ \vdots & \vdots & \ddots & \vdots \\ v_{N1}e^{i\varphi_{N1}} & v_{N2}e^{i\varphi_{N2}} & \dots & 1 \end{bmatrix}. \quad (\text{S43})$$

D. Measurement and correction of crosstalk

To compensation the crosstalk, we need to measure the total signal crosstalk matrix and perform

$$\mathbf{V}_d(t) = \mathbf{M}_{\mathbf{V}}^{-1} \tilde{\mathbf{V}}_d(t), \quad (\text{S44})$$

where $\mathbf{M}_{\mathbf{V}}^{-1}$ is the inverse matrix. However, in practice we cannot obtain $\mathbf{M}_{\mathbf{V}}$ directly, we need to characterize the crosstalk matrix of Rabi frequencies \mathbf{M}_{Ω} and calculate $\mathbf{M}_{\mathbf{V}}$ by using

$$\mathbf{M}_{\mathbf{V}} = \epsilon \mathbf{M}_{\Omega} \epsilon^{-1}, \quad (\text{S45})$$

where $\epsilon = \text{diag}\{\epsilon_{11}, \epsilon_{22}, \dots, \epsilon_{NN}\}$ and the crosstalk matrix of Rabi frequencies is defined as

$$\mathbf{M}_{\Omega} = \begin{bmatrix} 1 & c_{12}e^{i\varphi_{12}} & \dots & c_{1N}e^{i\varphi_{1N}} \\ c_{21}e^{i\varphi_{21}} & 1 & \dots & c_{2N}e^{i\varphi_{2N}} \\ \vdots & \vdots & \ddots & \vdots \\ c_{N1}e^{i\varphi_{N1}} & c_{N2}e^{i\varphi_{N2}} & \dots & 1 \end{bmatrix}. \quad (\text{S46})$$

where c_{ij} and φ_{ij} are the amplitude and phase crosstalk coefficients to be measured.

In the linear region of IQ mixer, we actually use Eq. (S19) to describe the relationship between Rabi frequency and the input IQ signals, and thus

$$\mathbf{M}_{\mathbf{V}_{\text{IQ}}} = \eta \mathbf{M}_{\Omega} \eta^{-1}, \quad (\text{S47})$$

where η is given by $\eta = \text{diag}\{\eta_1, \eta_2, \dots, \eta_N\}$ with η_i being the Rabi frequency of Q_i corresponding to the unit amplitude of IQ signals.

Now, we introduce an efficient method for characterizing c_{ij} and φ_{ij} in the crosstalk matrix \mathbf{M}_{Ω} . Let us take an example of Q_i . As shown in Fig. S9a, two resonant microwave signals $\omega_{d,i} = \omega_{d,j} = \omega_d$ are simultaneously input from the XY

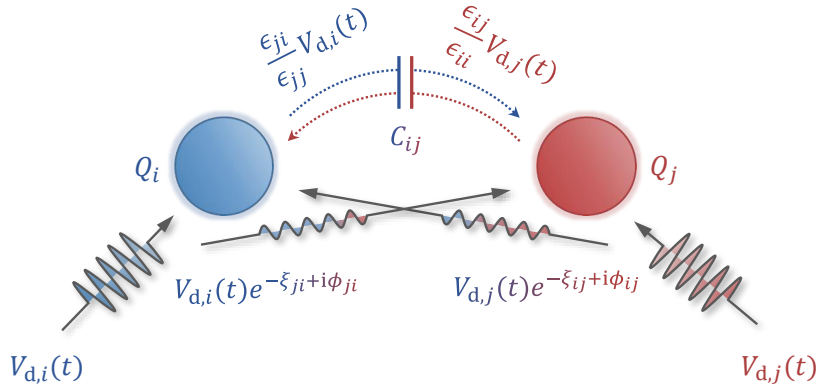


FIG. S8. **Schematic of microwave signal crosstalk.** Here, we take two qubits Q_i and Q_j as an example. Their individual driving voltages $V_{d,i}(t)$ and $V_{d,j}(t)$ induce two types of crosstalk. One type of crosstalk is due to the presence of coupling capacitance C_{ij} , which causes the crosstalk only in amplitude. The parameters ϵ_{ij} and ϵ_{ji} are explained in Eq. (S36), which depends on the coupling capacitance C_{ij} between the two qubits. The other type of crosstalk is caused by the propagation of microwave signals through the medium on the chip. According to electrostatics, it will lead to the crosstalk both in amplitude and phase. The parameters ξ and ϕ are the amplitude attenuation factor and phase retardation of microwave propagation, respectively.

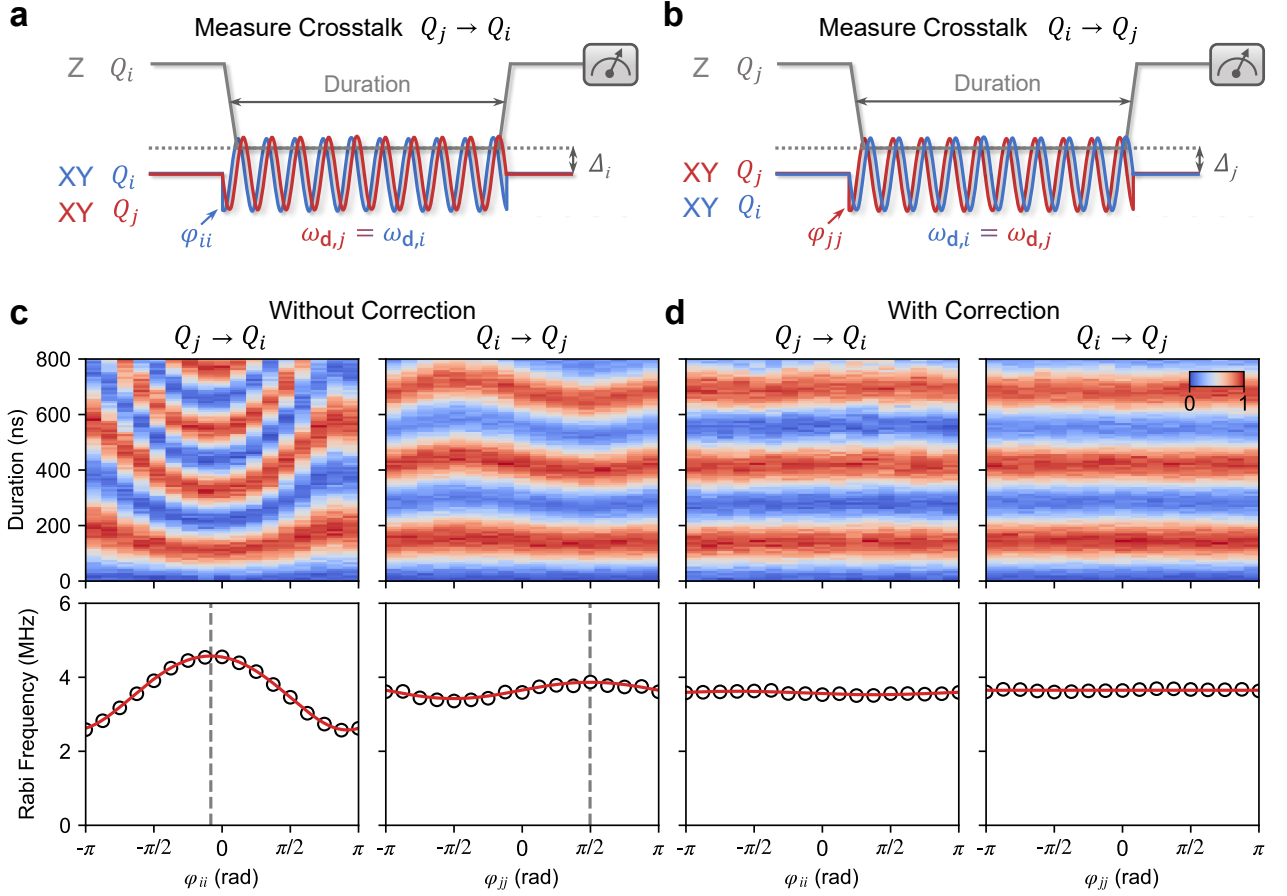


FIG. S9. **Measurement of the microwave crosstalk.** **a**, Experimental pulse sequence for measuring the crosstalk from Q_j to Q_i . **b**, Experimental pulse sequence for measuring the crosstalk from Q_i to Q_j . The parameters φ_{ii} and φ_{jj} denote the additional phases added into the XY control lines of Q_i and Q_j , respectively. The detuning between the qubit frequency and XY drive frequency is defined as $\Delta_q = \omega_q - \omega_{d,q}$, which is usually set to zero. **c**, Typical experimental data of measuring crosstalk without correction. **d**, Typical experimental data of measuring crosstalk with correction. The heatmap represents the probabilities of qubit in $|1\rangle$. The black hollow circle denotes the effective Rabi frequency obtained by fitting the Rabi oscillation. The red solid line is the result of fitting the effective Rabi frequency by using Eq. (S48). The grey dashed line implies the fitted crosstalk phase.

control lines of Q_i and Q_j . Meanwhile, Q_i is biased near the resonant frequency with the detuning $\Delta_i = \omega_i - \omega_{d,i}$. Due to the crosstalk, the effective Hamiltonian of Q_i under the rotation frame becomes $\hat{H}_d^{(i)} = \Delta_i \hat{\sigma}_i^+ \hat{\sigma}_i^- + (\tilde{\Omega}_i \hat{\sigma}_i^+ + \text{H.c.}) / 2$ with $\tilde{\Omega}_i = \Omega_i e^{-i\phi_i} + c_{ij} \Omega_j e^{i(\varphi_{ij} - \phi_j)}$, and the corresponding effective Rabi frequency is

$$\Omega_R^{(i)} = \sqrt{\Delta_i^2 + \Omega_i^2 + \Omega_{ij}^2 + 2\Omega_i \Omega_{ij} \cos(\varphi_{ij} - \varphi_{ii})}, \quad (\text{S48})$$

where $\Omega_{ij} = c_{ij} \Omega_j$ denotes the crosstalk Rabi frequency from Q_j to Q_i , and $\varphi_{ii} = \phi_j - \phi_i$ represents the additional XY phase added in Q_i relative to Q_j . By scanning φ_{ii} and measure the probabilities of Q_i in $|1\rangle$ as a function of the duration of XY drive, we can obtain $\Omega_R^{(i)}$. Using Eq. (S48) to fit the results of $\Omega_R^{(i)}$, we can determine the crosstalk coefficients c_{ij} and φ_{ij} . The procedure for determining c_{ji} and φ_{ji} is similar as long as we treat Q_j as Q_i . Here we show the partial crosstalk matrix between the 24 qubits used in experiments in Fig. S10.

Supplementary Note 4. THE EFFECT OF DECOHERENCE

In this section, we discuss the effect of decoherence. Since the conservation of the particle number is essentially important for the observation of spin hydrodynamics, we pay attention to the energy relaxation effect, characterized by the coherence time T_1 . To quantify the impact of decoherence on the particle number, we numerically simulate the dynamics of $n(t)$ by solving the

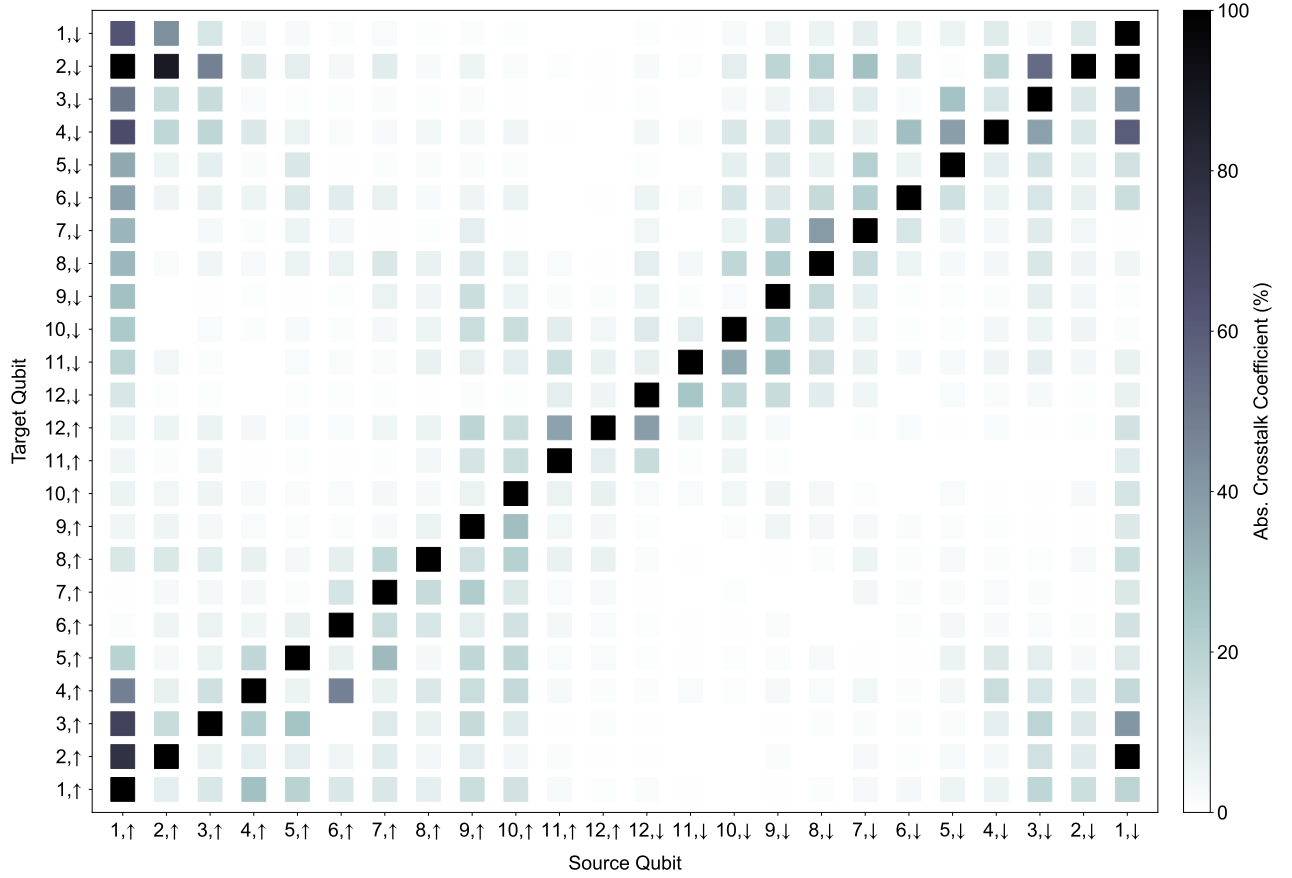


FIG. S10. **Partial crosstalk matrix of XY drive.** The heatmap represents the modulus of the crosstalk coefficient, namely $|c_{ij}|$. Here, we show the crosstalks between 24 qubits in the ladder.

Lindblad master equation

$$\frac{d\hat{\rho}(t)}{dt} = i[\hat{H}, \hat{\rho}(t)] + \sum_{j=1}^N (\hat{L}_j \hat{\rho}(t) \hat{L}_j^\dagger - \frac{1}{2} \{\hat{L}_j^\dagger \hat{L}_j, \hat{\rho}(t)\}), \quad (\text{S49})$$

where $\hat{\rho}(t) = |\psi(t)\rangle\langle\psi(t)|$ is the density matrix, \hat{H} is the Hamiltonian Eq. (1) in the main text, and $\hat{L}_j = \hat{\sigma}_j^- / \sqrt{T_1}$ represents the Lindblad operators for the energy relaxation, with T_1 being the energy lifetime.

For the numerical simulation, we adopt $T_1 = 32.1 \mu\text{s}$ based on the device information shown in Table. S1. Here, we consider a ladder with the number of qubits $N = 16$, and the same initial state shown in the inset of Fig. S2a. We employ the stochastic Schrödinger equation to efficiently solve the Lindblad master equation (S49). First, we study the dynamics of the particle number $\langle n(t) \rangle$ under the decoherence, and the results are plotted in Fig. S11a. With the evolved time $t = 200 \text{ ns}$, the value of $\langle n(t) / 2L \rangle$ is around 0.497, suggesting that decoherence does not significantly influence the conservation of the particle number. We then numerically demonstrate that decoherence does not strongly affect the dynamics of autocorrelation function $C_{1,1}(t)$ with the evolved time up to 200 ns, and the dynamics of $C_{1,1}(t)$ simulated by solving the Lindblad master equation (S49) is more or less the same to the unitary dynamics (see Fig. S11b).

Supplementary Note 5. XY DRIVE APPROACH TO GENERATE HAAR-RANDOM STATES

For the Haar-random state $|\psi^R\rangle$, we can define the probability with respect to the computational basis $|k\rangle$ as $p_k = |\langle k | \psi^R \rangle|^2$. It has been shown that the distribution of the probabilities $\{p = p_k\}$ will approximate the so-called Porter-Thomas distribution [35-37]

$$\text{Pr}(p) = D e^{-Dp}, \quad (\text{S50})$$

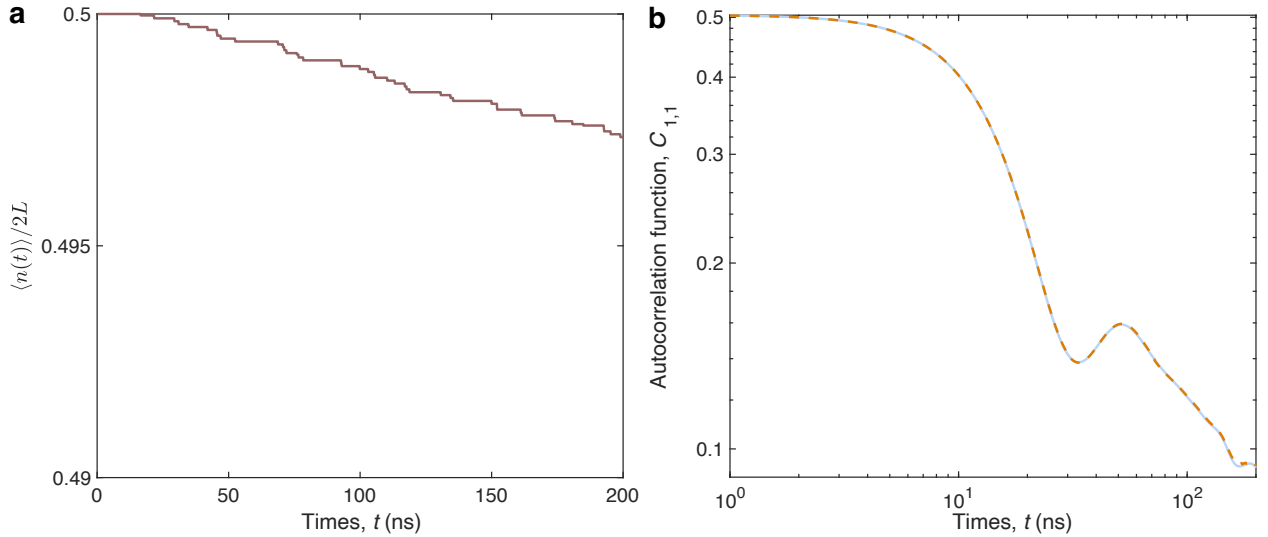


FIG. S11. **The effect of decoherence.** **a**, For the qubit ladder with a length $L = 8$ (the number of qubits $N = 16$), the dynamics of particle number $\langle n(t) \rangle$ with decoherence, i.e., energy relaxation, quantified by $T_1 = 32 \mu\text{s}$. **b**, The dynamics of autocorrelation function $C_{1,1}(t)$ with decoherence (dashed curve), in comparison with the unitary dynamics (solid curve).

where $D = 2^N$ is the total dimension of the Hilbert space. To generate the Haar-random states via the evolution \hat{U}_R in this experiment (seen in the main text or Fig. S12a), we bias the auxiliary qubit Q_A away from the resonance frequency and apply the XY drive pulses on all the remainder qubits Q_R participating in the resonance. The experimental pulse diagram is shown in Fig. S12b. After a time t_R , we perform joint readout of Q_R with N_s single-shot measurements to obtain the joint probabilities, and then calculate the participation entropy

$$S_{\text{PE}}(t_R) = - \sum_{k=1}^D p_k(t_R) \ln p_k(t_R), \quad (\text{S51})$$

where p_n is the joint probabilities of all $D = 2^N$ bitstrings. As shown in Fig. S12c, the participation entropy increases rapidly and then tends to a stable value. This value matches the participation entropy of the Haar-random state, namely

$$S_{\text{PE},|\psi^R\rangle} = -D \int_0^1 dp \Pr(p) p \ln p = \ln D - 1 + \gamma, \quad (\text{S52})$$

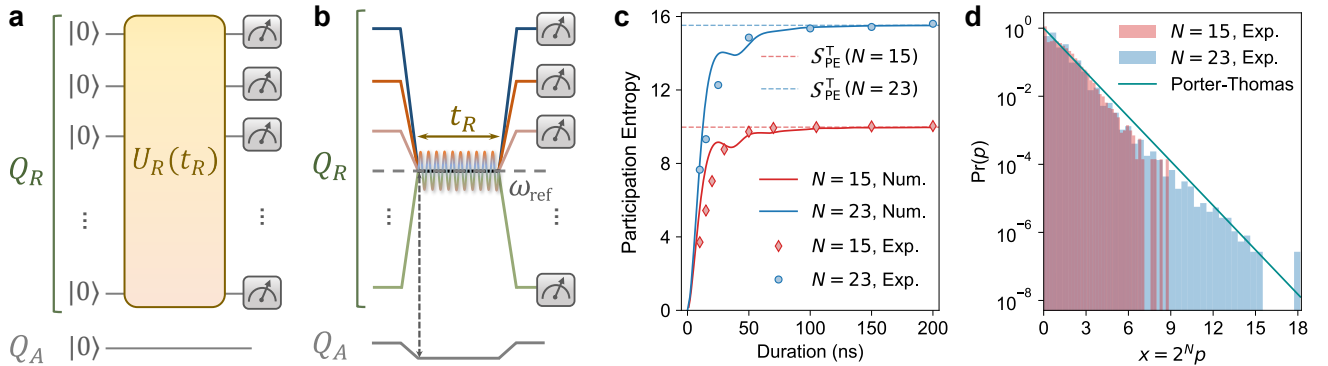


FIG. S12. **Generation and characterization of the XY drive approach to prepare the Haar-random states.** **a**, The schematic diagram of the quantum circuit. **b**, The corresponding experimental pulse sequence. We bias the auxiliary qubit Q_A away from the resonance frequency and apply the XY drive pulses on all the remainder qubits Q_R participating in the resonance at frequency $\omega_{\text{ref}} \approx 4.534 \text{ GHz}$, with a duration t_R . **c**, The evolution of participation entropy S_{PE} vs. the duration of XY drive. The dashed line represents the participation entropy of N -qubit Haar-random state. Here, we fix $Q_{1,\uparrow}$ as Q_A , and N is the total number of Q_R . **d**, The bitstring histogram of the measured $D = 2^N$ joint probabilities. The solid line shows the ideal results of Porter-Thomas distribution. For $N = 15$ and $N = 23$, we perform $N_s = 5 \times 10^5$ and $N_s = 3 \times 10^7$ single-shot measurements, respectively

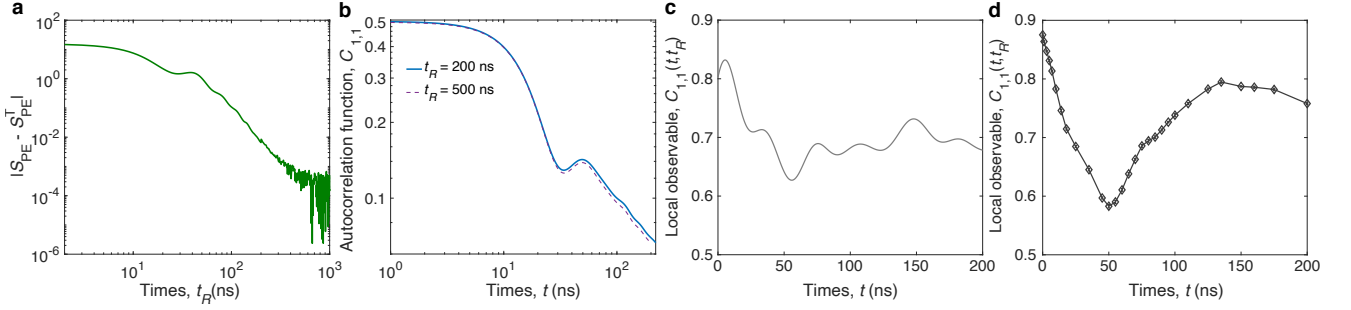


FIG. S13. **Impact of different t_R for generating Haar-random states.** **a**, The difference between the participation entropy at an evolved time t_R and that corresponding to Haar-random states S_{PE}^T , i.e., $|S_{PE}(t_R) - S_{PE}^T|$. **b**, The numerical results of autocorrelation function $C_{1,1}$ for the qubit ladder with $L = 12$, and different states generated from $\hat{U}_R(t_R)$ with $t_R = 200$ ns and 500 ns. **c**, The numerical simulation of the dynamics of the local observable $C_{1,1}(t_R, t)$ with a fixed $t_R = 15$ ns. **d**, The experimental data for the dynamics of the local observable $C_{1,1}(t_R, t)$ with a fixed $t_R = 15$ ns.

where $\gamma \approx 0.577$ is the Euler constant. The final state after a long-time evolution is therefore closer to a Haar-random state, which shows the Porter-Thomas distribution of the bitstring joint probabilities in the statistical histogram, see Fig. S12d. In the experiment, we select $t_R = 200$ ns to generate the Haar-random state and use this state as the initial state for subsequent interactions.

We note that the von Neumann entanglement entropy (EE) can also characterize the Haar-random states by achieving the Page value $S_{\text{Page}} \simeq \log m - m/2n$, where m and n represent the dimension of Hilbert space of the subsystem and the remainder, respectively. However, experimental measurement of EE requires additional single-qubit rotations, which can influence the accuracy of the results, especially for large system sizes. Here, we adopt the participation entropy, which can be directly measured by single-shot readout in z -direction, without rotations of qubits.

We now discuss the impact of different evolved time t_R for generating Haar-random states on the measurement of infinite-temperature autocorrelation function $C_{1,1}$. In Fig. S13a, we plot the numerical results of the difference between the participation entropy of the quenched state at $t = t_R$ and the participation entropy corresponding to the Haar-random state, i.e., $|S_{PE}(t_R) - S_{PE}^T|$ with the evolved time t_R up to $1 \mu\text{s}$. It can be seen that with $t_R \simeq 200$ ns, the difference reaches $|S_{PE}(t) - S_{PE}^T| \sim 10^{-1}$, and a lower difference can be achieved for longer evolved time t . However, as shown in Fig. S13b, the dynamical behaviors of autocorrelation function $C_{1,1}$, with the states generated by different evolved time of $\hat{U}_R(t_R)$ with $t_R \geq 200$ ns, do not have a significant change, which indicates that the evolved time $t_R \simeq 200$ ns is sufficient to generate a faithful Haar-random state for measuring the infinite-temperature spin transport.

We then extensively study the dynamics with short t_R . In this case, the state $|\psi^R\rangle$ is far away from Haar-random states, and the local observable $\langle \psi_\beta^R | \hat{\sigma}_\alpha^z(t) | \psi_\beta^R \rangle$, with $|\psi_\beta^R\rangle = \hat{U}_R(t_R) \otimes_{i \in Q_R} |0\rangle_i$, can no longer be approximate with the infinite-temperature correlation function $\text{Tr}[\hat{\sigma}_\alpha^z(t) \hat{\sigma}_\beta^z]/D$. Consequently, we denote the quantity as local observable $C_{1,1}(t_R, t)$, with t_R and t being the evolved time for $\hat{U}_R(t_R)$ and $\hat{U}_H(t)$ shown in the quantum circuit shown in Fig. 1c in the main text, respectively. In Fig. S13c and d, we plot the numerical and experimental data for the dynamics of the local observable $C_{1,1}(t_R, t)$ with a fixed short time $t_R = 15$ ns, respectively. For a small $t_R = 15$ ns, after an initial drop, the local observable has an oscillation around a value larger than 0.5. This can be explained by the fact that the state $|\psi^R\rangle$ is close to the initial state $|00\dots 0\rangle$ with small t_R , and when $t_R = 0$ and $t = 0$, actually, based on Eq. (3) of the main text, $c_{1,\uparrow;1,\uparrow} = c_{1,\uparrow;1,\downarrow} = c_{1,\downarrow;1,\downarrow} = c_{1,\downarrow;1,\uparrow} = 1$, which leads to the local observable $C_{1,1}(0, 0) = 1$.

Supplementary Note 6. FINITE-SIZE EFFECT FOR THE SPIN TRANSPORT IN THE CLEAN SUPERCONDUCTING QUBIT LADDER

In this section, we discuss the finite-size effect of the spin transport. We consider the clean superconducting qubit ladder without disorder or linear potential as an example, where the diffusive transport is expected to occur. We numerically simulate a long time evolution with the final time $t = 2000$ ns ($t\bar{J} \simeq 91.2$). As shown in Fig. S14, due to the finite-size effect, the $C_{1,1}(t)$ will saturate to a stable value for long time. The time interval with the power-law decay $C_{1,1} \propto t^{-z}$ becomes longer for larger L . For $L = 8$ and 12, the estimated time intervals with the power-law decay are $t \in [50 \text{ ns}, 170 \text{ ns}]$ and $t \in [50 \text{ ns}, 450 \text{ ns}]$ (highlighted by the arrows in Fig. S14), respectively. By fitting the numerical data in the time interval for $L = 8$ in $t \in [50 \text{ ns}, 140 \text{ ns}]$ and $L = 12$ in $t \in [50 \text{ ns}, 450 \text{ ns}]$, we obtain the exponent $z \simeq 0.45$ for $L = 8$ and $z \simeq 0.5$ for $L = 12$. In short, the signature of diffusive transport becomes more clear for larger system size.

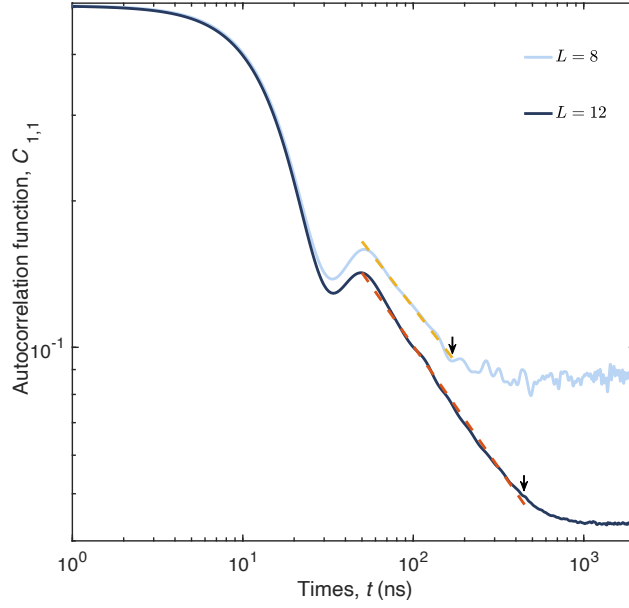


FIG. S14. **Finite-size effect.** Numerical simulation of the autocorrelation function $C_{1,1}(t)$ for the qubit ladder with different system sizes. For $L = 12$, the system consists of 24 qubits, i.e., $Q_{1,\uparrow}, \dots, Q_{12,\uparrow}$ and $Q_{1,\downarrow}, \dots, Q_{12,\downarrow}$. For $L = 8$, the system consists of 16 qubits, i.e., $Q_{1,\uparrow}, \dots, Q_{8,\uparrow}$ and $Q_{1,\downarrow}, \dots, Q_{8,\downarrow}$. The dashed lines show the power-law fitting of the numerical results in the time interval $t \in [50 \text{ ns}, 170 \text{ ns}]$ for $L = 8$ and $t \in [50 \text{ ns}, 450 \text{ ns}]$ for $L = 12$.

Supplementary Note 7. FINITE-TIME EFFECT FOR THE SPIN TRANSPORT IN DISORDERED SYSTEMS

Here, we consider a longer evolved final time $t = 600 \text{ ns}$, and study the impact of longer final time on the transport exponent z obtained by the power-law fitting $C_{1,1} \propto t^{-z}$. We focus on the disordered systems with $W/2\pi = 32 \text{ MHz}$ and 50 MHz . With the time window $t \in [50, 200] \text{ ns}$, as shown in the Fig. 3b of the main text, $z \simeq 0.02$ and $z \simeq 0.13$ for $W/2\pi = 50 \text{ MHz}$ and 32 MHz , respectively. With the time window $t \in [50, 600] \text{ ns}$, the fittings are shown in Fig. S15a with $z \simeq 0.03$ and $z \simeq 0.13$ for $W/2\pi = 50 \text{ MHz}$ and 32 MHz , respectively. It is seen that with the time window $t \in [50, 600] \text{ ns}$, the transport exponents z are slightly larger than those for the time window $t \in [50, 200] \text{ ns}$.

We also plot the transport exponent z obtained from the power-law fitting in the time interval $t \in [t_i, t_f]$, with a fixed initial time $t_i = 20 \text{ ns}$, and different t_f in Fig. S15b and c for $W/2\pi = 32 \text{ MHz}$ and 50 MHz , respectively. It is shown that with longer final time t_f , the transport exponent z exhibits a propensity to increase.

Supplementary Note 8. ADDITIONAL NUMERICS AND DISCUSSIONS

In this section, we numerically study another type of autocorrelation functions which are defined by the average over a product state $|\psi_0\rangle$. In the main text, we focus on the infinite-temperature autocorrelation function $C_{\mathbf{r},\mathbf{r}} = \text{Tr}[\hat{\rho}_{\mathbf{r}}(t)\hat{\rho}_{\mathbf{r}}]/D$ with D being the dimension of the Hilbert space. Alternatively, one can also consider the autocorrelation function average over a product state $|\psi_0\rangle$, i.e.,

$$C_{\mathbf{r},\mathbf{r}}(|\psi_0\rangle) = \langle \psi_0 | \hat{\rho}_{\mathbf{r}}(t) \hat{\rho}_{\mathbf{r}} | \psi_0 \rangle. \quad (\text{S53})$$

Here, we reveal that the autocorrelation function $C_{\mathbf{r},\mathbf{r}}(|\psi_0\rangle)$ cannot show generic properties of spin transport, and the dynamics of $C_{\mathbf{r},\mathbf{r}}(|\psi_0\rangle)$ is highly dependent on the choice of $|\psi_0\rangle$.

We consider the titled superconducting qubit ladder consisting of 24 qubits with $W_S/2\pi = 60 \text{ MHz}$, and the slope of the linear potential $\gamma/2\pi \simeq 11 \text{ MHz}$. Three chosen product states $|\psi_0\rangle$ for the autocorrelation function (S53) are shown in Fig. S16a. The product states with the domain wall number $n_{\text{dw}} = 10, 4$, and 2 are labeled as $|\psi_0^{(10)}\rangle$, $|\psi_0^{(4)}\rangle$, and $|\psi_0^{(2)}\rangle$, respectively. It can be directly calculated that the $\langle \psi_0^{(10)} | \hat{H} | \psi_0^{(10)} \rangle = \langle \psi_0^{(4)} | \hat{H} | \psi_0^{(4)} \rangle = \langle \psi_0^{(2)} | \hat{H} | \psi_0^{(2)} \rangle$. The results of the time evolution of $C_{\mathbf{r},\mathbf{r}}(|\psi_0\rangle)$ with $\mathbf{r} = 1$ are presented in Fig. S16b. It is seen that for the product state with $n_{\text{dw}} = 2$, the decay of $C_{\mathbf{r},\mathbf{r}}(|\psi_0\rangle)$ can be neglected, while the decay becomes stronger when we consider $C_{\mathbf{r},\mathbf{r}}(|\psi_0\rangle)$ with $n_{\text{dw}} = 4$ and 10 .

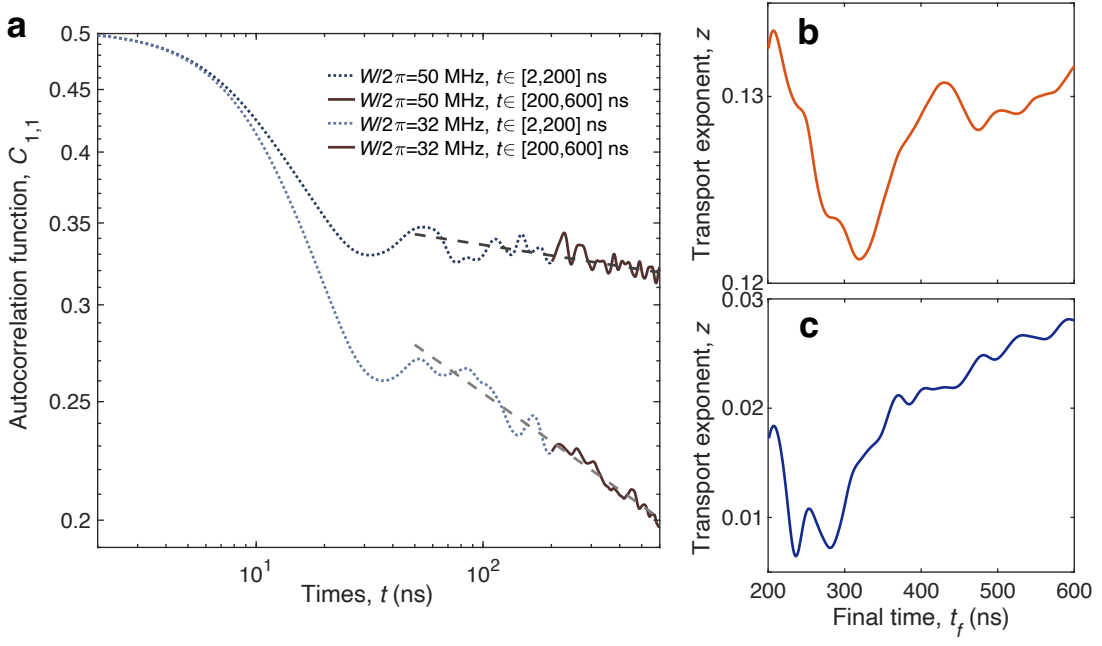


FIG. S15. **Impact of the finite-time effect.** **a**, Numerical results for the time evolution of autocorrelation function $C_{1,1}(t)$ for the qubit ladder with $L = 12$, and two values of disorder strengths $W/2\pi = 32$ MHz and 50 MHz. The evolved time is up to a longer time $t = 600$ ns. The dashed lines show the power-law fitting $C_{1,1} \propto t^{-z}$. **b**, For the disordered system with $W/2\pi = 32$ MHz, the transport exponent z obtained from the power-law fitting for the numerical results with the time interval $t \in [t_i, t_f]$, $t_i = 50$ ns, and different t_f . **c** is similar to **b**, but for the disordered system with $W/2\pi = 50$ MHz.

Actually, in ref. [15], it has been shown that the infinite-temperature autocorrelation function can be expanded as

$$C_{\mathbf{r},\mathbf{r}} = \frac{1}{D} \text{Tr}[\hat{\rho}_{\mathbf{r}}(t)\hat{\rho}_{\mathbf{r}}] = \frac{1}{D} \sum_{k=1}^D \langle k | \hat{\rho}_{\mathbf{r}}(t) \hat{\rho}_{\mathbf{r}} | k \rangle, \quad (\text{S54})$$

where $|k\rangle = |\sigma_{1,\uparrow}\sigma_{2,\uparrow}\dots\sigma_{12,\uparrow}; \sigma_{1,\downarrow}\sigma_{2,\downarrow}\dots\sigma_{12,\downarrow}\rangle$ is the product states in the σ^z basis. As shown in Fig. S16b, a single term $\langle k | \hat{\rho}_{\mathbf{r}}(t) \hat{\rho}_{\mathbf{r}} | k \rangle$ in (S54) cannot capture the properties of infinite-temperature spin transport. In our work, we employ the quantum circuit shown in Fig. 1c to directly measure the infinite-temperature autocorrelation function, without the need of sampling different product states.

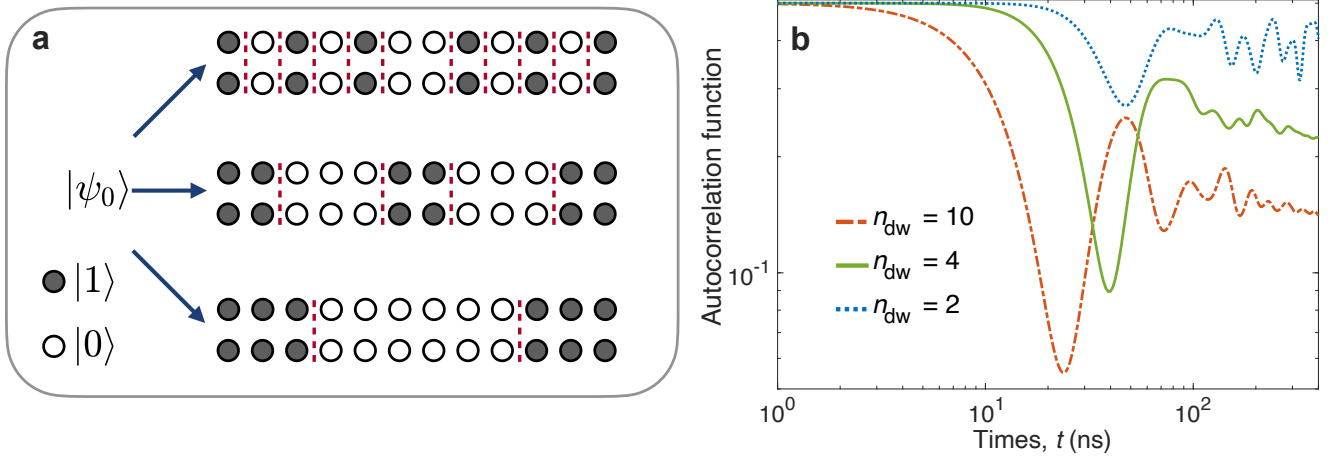


FIG. S16. **Additional numerical results for the spin transport on the titled superconducting qubit ladder.** **a**, Schematic diagram of three different product states $|\psi_0\rangle$ for the definition of the autocorrelation function $C_{1,1} = \langle \psi_0 | \hat{\rho}_1(t) \hat{\rho}_1 | \psi_0 \rangle$. From the top to bottom, the domain wall number of product states $|\psi_0\rangle$ is $n_{dw} = 10, 4,$ and $2,$ respectively. **b**, Time evolution of the autocorrelation function $C_{1,1} = \langle \psi_0 | \hat{\rho}_1(t) \hat{\rho}_1 | \psi_0 \rangle$ with the product states shown in **a** for the titled superconducting qubit ladder with $W_S/2\pi = 60$ MHz.